



## Reveals that electron transfer regime mediated by electron shuttle rather than adjacent transfer in B-doped 3D porous carbon framework: Exploration of interactions and identification of the main active site

Meng-Zhu Qin <sup>a</sup>, Yanyan Bian <sup>c</sup>, Huai-Yuan Niu <sup>b,\*</sup>, Wen-Xin Fu <sup>a</sup>, Xue-Gang Zhang <sup>a</sup>, Qi-Yao Hu <sup>a</sup>, Duan Guo <sup>a</sup>, Cheng-Gang Niu <sup>a,\*</sup>, Lei Zhang <sup>d</sup>

<sup>a</sup> College of Environmental Science and Engineering, Key Laboratory of Environmental Biology and Pollution Control, Ministry of Education, Hunan University, Changsha, China

<sup>b</sup> State Key Laboratory of Chemo/Biosensing and Chemometrics, College of Chemistry and Chemical Engineering, Hunan University, Changsha 410082, China

<sup>c</sup> Key Laboratory of Wood Materials Science and Utilization (Beijing Forestry University), Ministry of Education, Beijing 100083, China

<sup>d</sup> College of Chemistry and Chemical Engineering, Hunan University of Science and Technology, Xiangtan 411201, China



### ARTICLE INFO

#### Keywords:

B-doped porous carbon  
Peroxidisulfate  
Electron transfer  
Inner/outer-sphere interactions  
Charge-assisted hydrogen bonding

### ABSTRACT

The determination of non-radical pathways and identification of the main active site in the persulfate (PS) activation by B-doped carbonaceous materials are still controversial. Therefore, sodium citrate was selected as the carbon source and self-template for synthesizing a B-doped carbonaceous materials to activate peroxidisulfate (PDS) in this work. Multiple characterizations and experiments revealed that the electron transfer regime was responsible for the activation of PDS. On the one hand, the metastable surface complexes were generated due to the adsorption of PDS onto the catalyst surface via inner-sphere interaction. On the other hand, the interaction between BPA and the catalyst was verified as charge-assisted hydrogen bonding. In addition, BC<sub>3</sub> was identified as the main active site. Based on the detailed and in-depth exploration of the electron transfer regime during the PDS activation of B-doped carbonaceous materials, this work further elucidated interactions, and the vital role of BC<sub>3</sub> in PDS activation.

### 1. Introduction

Persulfate-based advanced oxidation processes (PS-AOPs) have attracted extensive attention and research due to their merits of high-efficient and broad-spectrum removal of organic micropollutants (OMPs). The mechanism of PS-AOPs mainly involves radical and non-radical pathways, depending on the reactive oxygen species (ROSs). In the radical pathway, the peroxide bond (O-O) of peroxomonosulfate (PMS) and PDS is cleaved to generate hydroxyl (·OH, 1.5–2.7 V vs. normal hydrogen electrode (NHE)), sulfate (SO<sub>4</sub><sup>2-</sup>, 2.5–3.1 V vs. NHE) and superoxide radicals (O<sub>2</sub><sup>·-</sup>, 2.4 V vs. NHE), which have extremely strong oxidizing power and can effectively mineralize OMPs into water (H<sub>2</sub>O) and carbon dioxide (CO<sub>2</sub>) [1–3]. However, the natural organic matters (NOM) and anions in the water matrix compete with OMPs to react with radical ROSs and possibly generate toxic by-products, thus reducing the degradation efficiency of OMPs and limiting the practical application of PS-AOPs [4]. Relatively, non-radical pathways involving singlet oxygen

(<sup>1</sup>O<sub>2</sub>), electron transfer regime, and high-valence metal/metal-oxo species have moderate oxidability, which can selectively degrade electron-rich organic contaminants (such as phenols and anilines) [5]. Moreover, non-radical pathways can be applied to a wider range of pH and have a certain resistance to water matrices containing natural organic pollutants and anions [6]. Therefore, non-radical pathways attract more research interest due to the aforementioned merits [7]. In non-radical pathways dominated PS-AOPs, metal-free carbonaceous materials can be an ideal platform for design because they can avoid secondary pollution problems caused by metal leaching from metal-based catalysts. Currently, engineering carbon allotropes, such as carbon nanotubes, biochar, graphene, porous carbon, etc., to become high-efficiency catalysts for non-radical dominated PS-AOPs has been widely studied and reported [8].

Nonmetallic elements (such as N, S, B, P etc.) doping, and correspondingly generated vacancies and defects are commonly effective strategies for tuning carbon network microstructure to enhance catalytic

\* Corresponding authors.

E-mail addresses: [hyniu@hotmail.com](mailto:hyniu@hotmail.com) (H.-Y. Niu), [cgniu@hnu.edu.cn](mailto:cgniu@hnu.edu.cn) (C.-G. Niu).

performance [9]. So far, N-doped carbonaceous materials have been intensively studied due to their outstanding catalytic activity [10]. Similarly, due to the difference in electronegativity, B is able to tailor the carbon network structure to break its electroneutrality, resulting in more active sites in the carbonaceous materials [11]. Furthermore, the carbonaceous materials were endowed with higher electrochemical properties, such as electrical conductivity, because of the doping of B [12,13]. However, relatively few investigations have been conducted on B-doped carbonaceous materials used for PS-AOPs. The exploration of the non-radical activation mechanism and identification of the main active site for PS activation in B-doped carbonaceous materials remain controversial. On the one hand, Liu et al. reported that  $\text{BCO}_2$  was the major adsorption site, and the electron transfer regime was responsible for sulfamethoxazole (SMX) degradation in the B-doped biochar/PDS system [14]. On the other hand, a study by Gao et al. using B-doped biochar with defects as active sites to activate PDS demonstrated that the oxytetracycline removal was due to electron transfer and generation of  ${}^1\text{O}_2$  [15]. The same controversy existed in the activation of PMS by B-doped other carbonaceous materials [16,17]. Therefore, the electron transfer mechanism of B-doped carbonaceous materials and the revelation of the corresponding active sites remain to be further investigated.

The electron transfer regime usually refers to the process by which surface active complexes generated by adsorption and activation of PS on the catalyst surface interact directly or indirectly with the target contaminants. Specifically, based on the conductivity of the catalyst, electron transfer mechanisms can be classified into two specific categories as follows: (i) the catalyst acts as a bridge for charge transfer, allowing electrons to be transferred from OMPs as an electron donor through the catalyst to the PS as an electron acceptor (electron shuttle); (ii) electrons directly transfer from contaminants to metastable surface complexes formed between PS and catalyst (adjacent transfer) [1,18]. Although studies on the electron transfer regime confirmed to be the main oxidation mechanism in PS-AOPs have been widely reported to date, few studies specifically distinguish whether the electron transfer mechanism belongs to electron shuttle or adjacent transfer [1,19]. This is mainly because electrochemical characterization (open circuit potential, linear voltammetry curve, chronoamperometry, etc.), infrared and in situ Raman spectra are insufficient to differentiate between electron shuttle and adjacent transfer [18,20]. Based on discerning the specific electron transfer mechanism (electron shuttle or adjacent transfer), it is of significance to simultaneously explore the interactions (inner-sphere or outer-sphere interactions) between the catalyst and OMPs/PS to gain deeper insights into the catalytic mechanism. The inner-sphere interaction is a strong interaction, usually with a covalent bond, a combination of covalent and ionic bonds [21]. Comparatively, the strength in outer-sphere interaction is weaker, and van der Waals interaction and hydrogen bond are typical outer-sphere interactions [22,23]. At present, researches on the interactions mostly focused on metal oxide catalysts or carbonaceous catalysts loaded with metals [24,25]. In contrast, the interactions between metal-free carbonaceous catalysts and PS as well as OMPs have been relatively little studied [26]. Therefore, for metal-free carbonaceous catalysts, studying interactions between catalysts and PS/OMPs in the PS-AOPs system is an urgent gap that needs to be filled to gain a deeper understanding of the catalytic mechanism.

Considering the lower cost (\$0.74 per kg vs. \$2.2 per kg of PMS) and greater application potential of PDS, we adopt PDS as the target oxidant [21]. In this work, phenolic pollutants were chosen for use as target pollutants to evaluate catalytic activity. A B-doped 3D porous carbon framework interconnected with 2D graphite nanoplates (3D PCFGN) was synthesized and used for PDS activation. Free radicals quenching experiments, chemical probes experiments, attenuated total reflectance-Fourier transform infrared spectroscopy (ATR-FTIR) and Raman characterizations, and electrochemical characterizations were all performed stepwise to verify that the electron transfer mechanism dominated the degradation of phenolic contaminants. X-ray

photoelectron spectroscopy (XPS), field emission scanning electron microscope (FESEM) images, and density functional theory (DFT) calculations were employed to reveal the major active site. The electro-oxidation electrochemical device was constructed to specifically distinguish whether the electron transfer regime belonged to electron shuttle or adjacent transfer. Interactions between B-doped 3D PCFGN and PDS as well as BPA were disclosed by conducting ionic strength experiments, DFT calculations, effects of pH on BPA removal efficiency, and Zeta potentials of the B-doped 3D PCFGN. This work is devoted to the in-depth study of the electron transfer regime, which has a certain reference value for the demonstration of the non-radical mechanism in PS-AOPs in the future.

## 2. Experimental materials and methods

### 2.1. Chemicals and reagents

Potassium peroxydisulfate (PDS,  $\text{K}_2\text{S}_2\text{O}_8$ , ≥99.5%), trisodium citrate dihydrate (Na-Citrate,  $\text{C}_6\text{H}_5\text{Na}_3\text{O}_7 \cdot 2 \text{H}_2\text{O}$ , ≥99.0%), methyl alcohol ( $\text{MeOH}$ ,  $\text{CH}_4\text{O}$ , ≥99.5%), absolute ethyl alcohol ( $\text{EtOH}$ ,  $\text{C}_2\text{H}_5\text{O}$ , ≥99.7%), tert-butanol (TBA,  $\text{C}_4\text{H}_{10}\text{O}$ , ≥99.0%), p-benzoquinone (p-BQ,  $\text{C}_6\text{H}_4\text{O}_2$ , ≥98.0%), L-histidine ( $\text{C}_6\text{H}_9\text{N}_3\text{O}_2$ ), potassium iodide (KI, ≥99.0%), sodium hydrogen carbonate ( $\text{NaHCO}_3$ , ≥99.5%), sodium chloride ( $\text{NaCl}$ , ≥99.5%), anhydrous sodium carbonate ( $\text{Na}_2\text{CO}_3$ , ≥99.8%), potassium dihydrogen phosphate ( $\text{KH}_2\text{PO}_4$ , ≥99.5%), phosphoric acid ( $\text{H}_3\text{PO}_4$ , ≥85.0%), sulfuric acid ( $\text{H}_2\text{SO}_4$ , ≥98.0%), sodium hydroxide ( $\text{NaOH}$ , ≥96.0%), benzoic acid (BA,  $\text{C}_7\text{H}_6\text{O}_2$ , ≥99.5%), nitrobenzene (NB,  $\text{C}_6\text{H}_5\text{NO}_2$ , ≥99.0%) were purchased from Sinopharm Chemical Reagent Co., Ltd. Anhydrous sodium sulfate ( $\text{NaSO}_4$ , ≥99.5%), formic acid ( $\text{CH}_2\text{O}_2$ , ≥88.0%, HPLC), acetic acid ( $\text{C}_2\text{H}_4\text{O}_2$ , ≥99.8%, HPLC) were purchased from Kermel Chemical Reagent Co., Ltd. Boric oxide ( $\text{B}_2\text{O}_3$ , ≥98.0%), humic acid (HA,  $\text{C}_9\text{H}_9\text{NO}_6$ , 90% fulvic acid), ammonium acetate ( $\text{C}_2\text{H}_7\text{NO}_2$ , ≥99.0%, HPLC) were purchased from Rhawn Chemical Reagent Co., Ltd. Bisphenol A (BPA,  $\text{C}_{15}\text{H}_{16}\text{O}_2$ , ≥99.0%) was purchased from Xiya Chemical Reagent Co., Ltd. p-Chlorophenol (4-CP,  $\text{C}_6\text{H}_5\text{OCl}$ , ≥99.0%), o-chlorophenol (2-CP,  $\text{C}_6\text{H}_5\text{OCl}$ , ≥99.0%), 2, 4-dichlorophenol (2,4-DCP,  $\text{C}_6\text{H}_4\text{Cl}_2\text{O}$ , ≥98.0%), 2,4,6-trichlorophenol (2,4,6-TCP,  $\text{C}_6\text{H}_3\text{Cl}_3\text{O}$ , ≥98.0%) were purchased from Macklin Chemical Reagent Co., Ltd. Furfuryl alcohol (FFA,  $\text{C}_5\text{H}_6\text{O}_2$ , ≥98.0%) was purchased from Aladdin Chemical Reagent Co., Ltd. Deuterium oxide ( $\text{D}_2\text{O}$ , ≥99.9%) was purchased from Innochem Chemical Reagent Co., Ltd. Pure amorphous boron (A-boron) and crystal boron (C-boron) were obtained from Hebei Xintie Metal Materials Co., Ltd.

### 2.2. Preparation and characterizations of 3D PCFGN

A self-template method was employed to synthesize B-doped 2D carbon nanosheets. Typically, 15 mg Na-Citrate was pyrolyzed at 700 °C under Ar for 2 h at a heating rate of 5 °C/min. The reasons for choosing a pyrolysis temperature of 700 °C are detailed in Table S1. In order to fully dissolve the sodium salt produced during pyrolysis, the prepared black blocks were transferred to a beaker containing 500 mL of water and heated to 80 °C in a deionized water bath until the blocks dispersed into small black particles. After cooling, the obtained small black particles were washed three times with ethanol and deionized water, respectively, to remove tar and sodium salts produced during pyrolysis. The separated black powders were then dried in a vacuum oven at 60 °C overnight and denoted as Na-Citrate carbon nanosheets (NC).

A certain proportion of NC and  $\text{B}_2\text{O}_3$  (1: 4, 1: 5, 1: 6, and 1: 7) were weighed and placed in a beaker containing 100 mL of deionized water and heated to 80 °C in a water bath to ensure full dissolution of  $\text{B}_2\text{O}_3$ . The mixed solution was transferred to a Teflon-lined autoclave and hydrothermally heated at 160 °C for 18 h. After cooling, separation, and drying, the black powders were denoted as hydrothermal B-doped carbon nanosheets (HBC). The prepared HBC was calcined at a certain

temperature (800, 850, and 900 °C) for 2 h at an annealing rate of 5 °C/min in Ar. The calcined product was denoted as B-doped 2D carbon nanosheets (BC). (x-1) in BC(x-1) represented the mass ratio of  $\text{B}_2\text{O}_3$  to NC (x = 4, 5, 6 and 7). The HBC was thermally annealed in air at 400 °C for 30, 60, 90, and 120 min to obtain a series of catalysts. Milli-Q water was used in all experiments. Characterizations of 2D carbon nanosheet-based catalysts were described in detail in Text S1.

### 2.3. Experimental procedure

Bisphenol A (BPA) was selected as the target pollutant. Batch experiments were performed in a 250 mL beaker containing 100 mL of BPA solution (0.1 mM,  $\text{pH} = 6.5 \pm 0.1$ ) at room temperature ( $23 \pm 2$  °C). The initial pH of the solution was not controlled unless otherwise specified. Then, a certain amount of catalyst and PDS were simultaneously added to the beaker to initiate the reaction. At specified time intervals, 0.8 mL of the sample solution was extracted through a 0.42 μm filter and injected into a liquid phase vial containing 0.2 mL of methanol. The initial pH of the solution was adjusted with 0.1 M NaOH and 0.1 M  $\text{H}_2\text{SO}_4$  when evaluating the effects of the pH on BPA degradation. All experiments were performed in triplicates, and corresponding mean values and standard deviations were exhibited in the figures. The degradation efficiency of contaminants and decomposition efficiency of PDS were estimated by Eq. (1). The apparent reaction rate constant ( $k_{\text{obs}}$ ) can be calculated by Eq. (2). The Arrhenius formula (Eq. (3)) was used to calculate the activation energy ( $E_a$ ).

$$\text{The degradation/decomposition efficiency} (\%) = 100 \times (C_0 - C)/C \quad (1)$$

$$\ln(C/C_0) = -k_{\text{obs}} \times t \quad (2)$$

$$\ln k_{\text{obs}} = -\frac{E_a}{RT} + \ln A \quad (3)$$

where C and  $C_0$  represent the concentration at time t and 0. A stands for the Arrhenius constant. R is the molar gas constant ( $8.314 \text{ J mol}^{-1} \text{ K}^{-1}$ ), and T represents the reaction temperature.

### 2.4. Analytical methods

The concentrations of BPA, phenol, 4-CP, 2-CP, 2,4-DCP, 2,4,6-TCP, BA, NB, and FFA were measured via HPLC (Agilent 1260 Infinity II, USA) with an Agilent SB-C18 column ( $4.6 \times 250 \text{ mm}, 5 \mu\text{m}$ ). The HPLC analytical methods of the above-mentioned organic compounds are presented in Table S2. The concentration of PDS was determined via using a little modification of the method of Liang et al. (Text S3) [27]. The detailed computational methodology was listed in Text S2. ATR-FTIR and Raman analysis procedures were described in Text S4-S5. Intermediates of BPA during degradation were measured by UHPLC-MS (Agilent, USA). The detailed determination method was presented in Text S6. The zeta potentials of the prepared catalysts were analyzed by a nano-particle size ZETA potential analyzer (NaNoZS, Malvern, UK). TOC analyzers (Shimadzu, Japan) were used to measure total organic carbon (TOC) in water samples.

## 3. Results and discussion

### 3.1. Characterization of the B-doped 3D PCFGN

The X-ray diffraction (XRD) patterns of all prepared samples exhibited broad peaks at 2Theta at 25° and 43.3°, corresponding to (002) and (101) diffraction of 2 H graphite (JDPDF No. 74-2329) (Figs. 1a and S1) [28]. The microstructure and morphology of all synthesized catalysts presented a 3D PCFGN (Figs. 1b-e, S2 and S3). The elemental mapping and Energy Dispersive X-Ray (EDX) spectra of BC (5-1) illustrated the successful doping of B (Fig. S4 and S5). In addition, the doped B was uniformly distributed on the surface of 2D graphite (Table S3, Fig. S4). Benefiting from the abovementioned structure, the prepared composites have higher specific surface areas (Table S4 and Fig. S7). The surface chemical compositions of the catalysts were analyzed by X-ray photoelectron spectroscopy (XPS). The peaks of C, B and O elements were located at 284.8, 192.6 and 534.2 eV in the XPS full XPS survey spectra, respectively, further revealing that B was successfully doped into the  $\text{sp}^2\text{C}$  network (Fig. S6a). The high ratio of

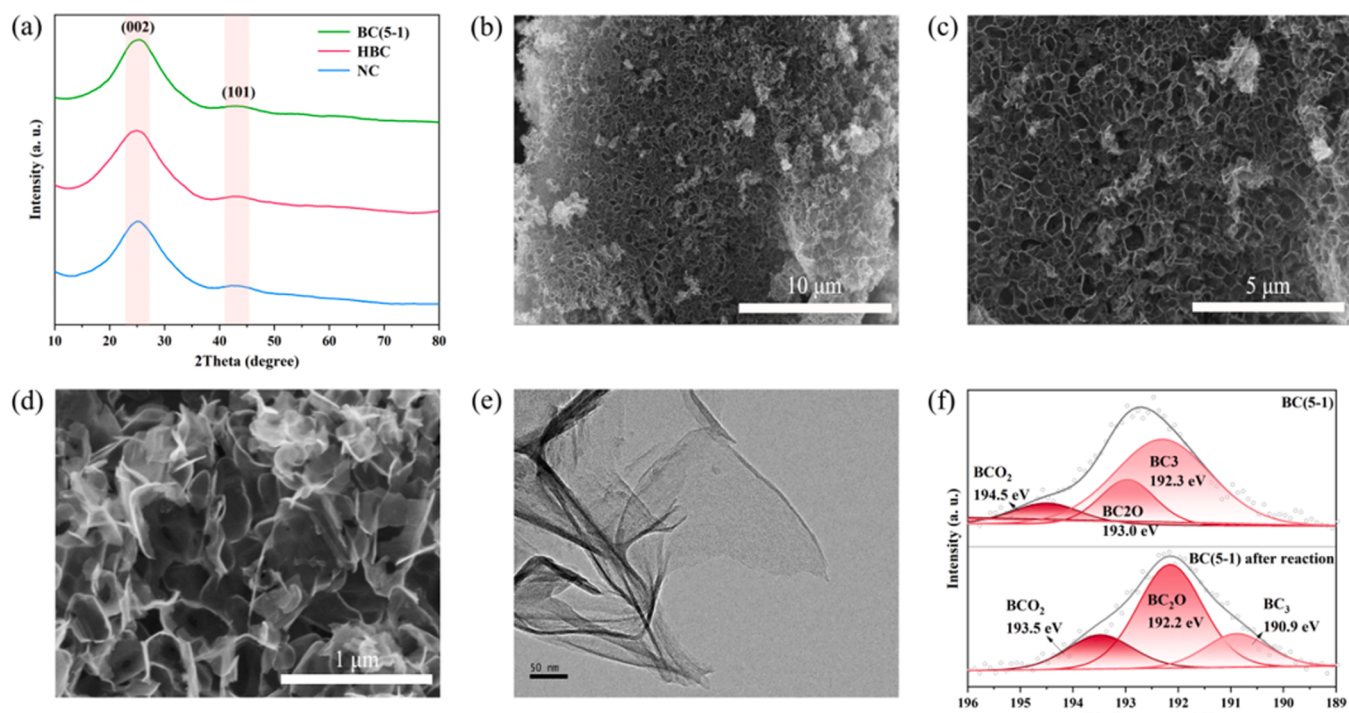


**Fig. 1.** (a) XRD patterns of NC, HBC and BC(5-1); (b-d) SEM and (e) transmission electron microscopy (TEM) images of BC(5-1); (f) B1s XPS spectra of BC(5-1) and BC(5-1) after reaction.

$\text{sp}^2\text{C}/\text{C}-\text{O}-\text{C}$  indicated that B-doped 3D PCFGN was mainly composed of C atoms, which was beneficial to improve the conductivity, thereby enhancing its electron transfer ability (Fig. S6b) [29]. Fig. 1f exhibited B1s XPS spectra with three peaks distributed at 194.5, 193.0 and 192.3 eV [12]. The higher binding energies of B1s in this work compared to other B-doped carbons further indicate that B was successfully doped into the 2D hexagonal graphite carbon network with the highest proportion of  $\text{BC}_3$  [14,30]. Notably, it has been reported that compared with  $\text{BC}_2\text{O}$  and  $\text{BCO}_2$ , the  $\text{BC}_3$  conformation with a graphite-like structure has higher conductivity, which was more conducive to improving the electron transfer efficiency [11,31].

### 3.2. Catalytic performance of BC(5–1)

As a comparison, the catalytic activity of undoped NCs was poor ( $0.0452 \text{ min}^{-1}$ ) (Fig. 2a). The BPA degradation performance of BC(5–1) ( $0.0960 \text{ min}^{-1}$ ) was higher than that of HBC ( $0.0456 \text{ min}^{-1}$ ), which may be due to the decrease of O content and increase of  $\text{BC}_3$  after secondary pyrolysis, thereby elevating conductivity of the catalyst (Fig. 2a) [12]. The catalytic performance of the catalysts prepared with different B/C ratios, calcination temperatures, PDS concentrations and catalyst dosages were further investigated. As shown in Figs. S8–S11, the catalyst with a B/C ratio of 5:1, calcination of  $800^\circ\text{C}$  and a dosage of 10 mg, and PDS concentration with 3 mM presented the best catalytic performance (94.04% within 30 min). Therefore, the BC(5–1)/PDS system was used for subsequent studies. The degradation of BPA by PDS alone was almost negligible (Fig. 2a). Only 12% of BPA was adsorbed by BC(5–1) within 30 min (Fig. S11b). The BC/PDS system showed a high degradation

efficiency for BPA, indicating that BC(5–1) has excellent activation ability for PDS.

In previous studies, boron alone was able to activate persulfate to degrade phenol [32]. Therefore, under the experimental conditions of this study, different boron species, such as A-boron, C-boron, and  $\text{B}_2\text{O}_3$ , were used to activate PDS for the degradation of BPA. Neither A-boron nor C-boron could activate the PDS to degrade the contaminants (Fig. S12), which was consistent with the study of Duan et al. [33]. Additionally, PDS was not activated by  $\text{B}_2\text{O}_3$  to degrade BPA (Fig. S12). Interestingly, the B-doped carbonaceous catalysts (HBC: after hydrothermal synthesis, BC(5–1): hydrothermal and secondary pyrolysis in turn) all showed better BPA degradation performance (Fig. S12). Fig. S12 indicated that the bonding between B and C atoms rather than individual boron and  $\text{B}_2\text{O}_3$  contributed to the PDS activation [34].

In order to investigate the difference in performance between physical mixtures and doped materials, we conducted experiments on BPA degradation by physical mixtures of NC + HBC, NC + A-boron, NC + C-boron, and NC +  $\text{B}_2\text{O}_3$ . Based on the ratio of C to B in the EDX results (Table S3 and Fig. S5), NC + A-boron (9.1 + 0.9 mg), NC + C-boron (9.1 + 0.9 mg), NC +  $\text{B}_2\text{O}_3$  (7.1 + 2.9 mg) were calculated for physical mixing, respectively. When 5 mg of NC and 5 mg of HBC were weighed for physical mixing, the BPA degradation efficiency was 74.46%, which was much smaller than the value of the doped BC(5–1) (94.04% in 30 min) (Fig. S13a). By further increasing the proportion of B in the physical mixture, such as NC + A-boron (5 + 5 mg), NC + C-boron (5 + 5 mg) and NC +  $\text{B}_2\text{O}_3$  (5 + 5 mg), the degradation efficiency of BPA was reduced to 35.04–37.71% (Fig. S13b). The experimental results of physical mixtures illustrated that the doped material/PDS

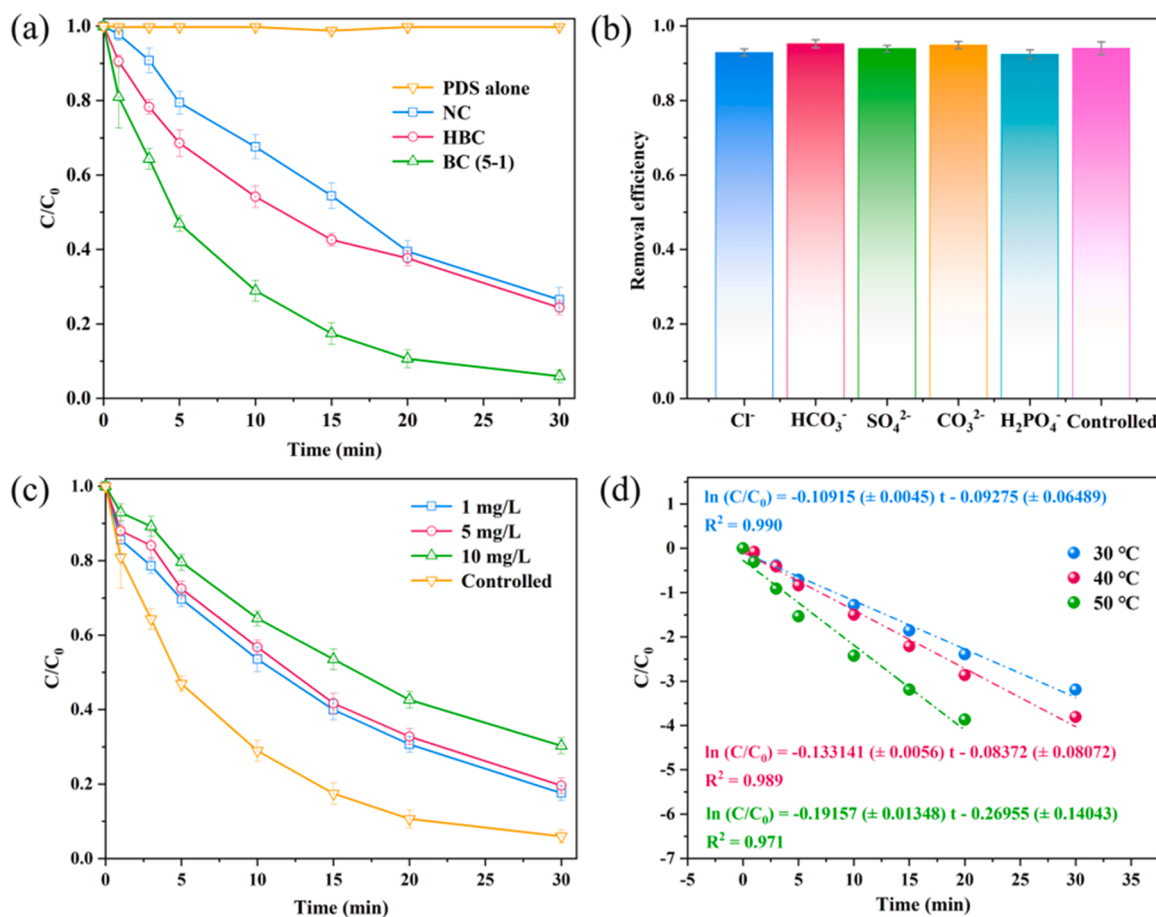


**Fig. 2.** (a) Catalytic activities of catalysts at different stages of synthesis; Effect of (b) common anions, (c) HA, and (d) reaction temperature on BPA degradation in BC(5–1)/PDS system. Reaction conditions: [BPA] = 0.1 mM, [PDS] = 3 mM, [catalyst] = 0.1 g/L, [temp] =  $23 \pm 2^\circ\text{C}$ , initial pH =  $6.5 \pm 0.1$ ,  $[\text{Cl}^-] = [\text{HCO}_3^-] = [\text{SO}_4^{2-}] = [\text{CO}_3^{2-}] = [\text{H}_2\text{PO}_4^-] = 1 \text{ mM}$ .

system degraded BPA better than the physical mixture/PDS system (Fig. S13).

In addition to investigating the catalytic activity of the BC(5–1)/PDS/BPA system, the abilities of the BC(5–1)/PDS/BPA system to resist various aqueous matrices were further investigated. Anions in the aqueous matrix compete with organic pollutants for free radicals, so the degradation efficiency of pollutants will be inhibited in radical pathways dominated AOPs [35]. However,  $\text{Cl}^-$ ,  $\text{HCO}_3^-$ ,  $\text{SO}_4^{2-}$ ,  $\text{CO}_3^{2-}$ , and  $\text{H}_2\text{PO}_4^-$  have little effect on BPA degradation efficiency (Fig. 2b). When the concentration of the common anions increased to 5 mM, the degradation of BPA was slightly inhibited, but the overall removal efficiency was still higher than 85% within 30 min (Fig. S14). The removal performance of BPA decreased with increasing HA concentration, which might be due to the higher affinity of HA with rich functional groups for BC compared to BPA and PDS (Fig. 2c). When the reaction temperature gradually increased, the degradation rate of BPA accelerated (Fig. 2d). The activation energy calculated according to Eq. (3) was  $22.83 \text{ kJ} \cdot \text{mol}^{-1}$ , which was significantly lower than that of the previously reported B-doped biochar ( $63.75 \text{ kJ} \cdot \text{mol}^{-1}$ ) and porous carbon ( $60.04 \text{ kJ} \cdot \text{mol}^{-1}$ ), indicating the excellent catalytic ability of BC(5–1) [14,16]. Other than that, the BC(5–1)/PDS system had strong adaptability to different water matrixes (Fig. S15).

### 3.3. Identification of electron transfer regime

BA and NB are frequently utilized as chemical probes to verify the presence of free radicals in PS-AOPs (Table S5). As shown in Fig. 3a, the removal efficiency of BA and NB reached 22.4% and 56.7% within 30 min, respectively. However, according to the secondary reaction rates of BA and NB with ·OH and  $\text{SO}_4^{2-}$  (Table S5), when there exist ·OH and  $\text{SO}_4^{2-}$  in the reaction system, the removal efficiency of BA will be higher than that of NB. Therefore, adsorption experiments of BA and NB were carried out. The adsorption efficiencies of BA and NB reached 22.5% and 56.2%, respectively, which were almost equal to their

respective removal rates, indicating that BA and NB were barely degraded (Fig. S16). From this, it was preliminarily judged that there was almost no ·OH and  $\text{SO}_4^{2-}$  in the BC(5–1)/PDS system.

Quenching experiments and EPR were also performed to identify the dominant ROS in BC(5–1)/PDS system. MeOH is commonly used to scavenge ·OH and  $\text{SO}_4^{2-}$  while TBA is chosen as a quenching agent for ·OH rather than  $\text{SO}_4^{2-}$  ( $k_2(\text{MeOH}, \cdot\text{OH}) = 9.8 \times 10^8 \text{ M}^{-1} \text{ s}^{-1}$ ,  $k_2(\text{MeOH}, \text{SO}_4^{2-}) = 2.5 \times 10^7 \text{ M}^{-1} \text{ s}^{-1}$ ,  $k_2(\text{TBA}, \cdot\text{OH}) = 5.2 \times 10^{10} \text{ M}^{-1} \text{ s}^{-1}$ ,  $k_2(\text{TBA}, \text{SO}_4^{2-}) = 8.4 \times 10^5 \text{ M}^{-1} \text{ s}^{-1}$ ) [36,37]. The addition of MeOH had little effect on the degradation of BPA, indicating that there was almost no ·OH and  $\text{SO}_4^{2-}$  in the BC(5–1)/PDS system (Fig. 3b). Even when the molar ratio of MeOH to PDS reached 1000, the degradation of BPA remained unaffected, which further reflected the absence of ·OH and  $\text{SO}_4^{2-}$  in the reaction system (Fig. S17a). However, the degradation performance of BPA was slightly inhibited after the addition of TBA and decreased with the increase of TBA concentration (Figs. 3b and S17b). This phenomenon contradicted the experimental results using MeOH scavenging. This might be because TBA has a higher affinity for the catalyst surface, which caused TBA to compete with BPA for adsorption on the BC(5–1) surface, thereby further inhibiting the degradation of BPA [24]. In addition, DMPO-·OH could also be formed by one step single electron transfer in the absence of ·OH (Figs. 3c and S18a). Combined with verification of chemical probes, free radicals quenching experiments, and EPR spectra, it was shown that there might be a single electron transfer pathway in BC(5–1)/PDS system.

The contribution of  $\text{O}_2^-$  can be determined by p-BQ and  $\text{CO}_3^{2-}$  as scavengers ( $k_2(p\text{-BQ}, \text{O}_2^-) = 2.9 \times 10^9 \text{ M}^{-1} \text{ s}^{-1}$ ,  $k_2(\text{CO}_3^{2-}, \text{O}_2^-) = 5 \times 10^8 \text{ M}^{-1} \text{ s}^{-1}$ ) [37]. In the presence of p-BQ, the degradation efficiency of BPA decreased from 94.0% to 18.7% in 30 min. Nevertheless, the degradation of BPA was not inhibited after the addition of  $\text{CO}_3^{2-}$ , which also acted as a superoxide radical scavenger (Figs. 3b, 2b, and S14). It was very likely that p-BQ reacted with PDS. Therefore, the decomposition of PDS in the presence of scavengers was carried out. It was evident from Fig. S19a that p-BQ consumes PDS in the system, thereby reducing

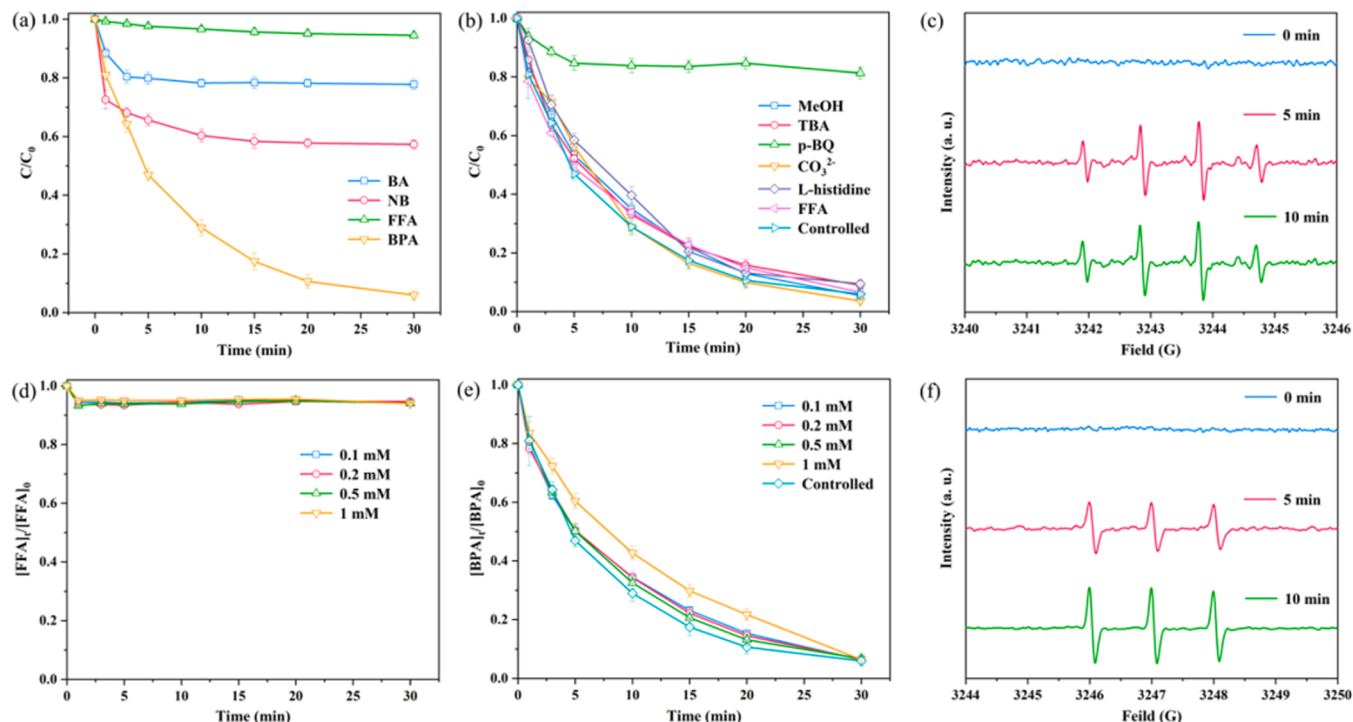


**Fig. 3.** (a) Removal of chemical probes, (b) quenching experiments in BC(5–1)/PDS system; EPR spectra of (c) ·OH and  $\text{SO}_4^{2-}$ , and (f)  $^1\text{O}_2$  in BC(5–1)/PDS/BPA system for 0, 5, 10 min; Removal of (d) FFA and (e) BPA under the coexistence of different concentrations of FFA. Reaction conditions:  $[\text{BA}] = [\text{NB}] = [\text{FFA}] = [\text{BPA}] = 0.1 \text{ mM}$ ,  $[\text{PDS}] = 3 \text{ mM}$ ,  $[\text{catalyst}] = 0.1 \text{ g/L}$ ,  $[\text{temp}] = 23 \pm 2^\circ\text{C}$ , initial  $\text{pH} = 6.5 \pm 0.1$ ,  $[\text{MeOH}] = [\text{TBA}] = 0.3 \text{ M}$ ,  $[\text{p-BQ}] = [\text{CO}_3^{2-}] = 5 \text{ mM}$ ,  $[\text{L-histidine}] = 30 \text{ mM}$ ,  $[\text{DMPO}] = [\text{TEMP}] = 100 \text{ mM}$ .

the initial concentration of PDS to inhibit the removal of BPA. Besides, it has been reported that BQ itself was highly oxidative, making it more likely that BQ adsorbed on the surface of carbon materials due to its hydrophobicity and acted as an electron acceptor to receive electrons from OMPs [38]. Moreover, the injection of nitrogen into the reaction system did not affect the degradation of BPA (Fig. S19b). It was concluded that the contribution of superoxide radicals to the reaction system was limited.

BPA still maintained higher degradation efficiency in complex aqueous matrices, suggesting that activation of PDS may not involve free radicals.  $^1\text{O}_2$ , as a member of non-radical ROSSs, possibly participated in the oxidation of BPA. L-histidine is a commonly used scavenger in  $^1\text{O}_2$  quenching experiments because of its high secondary reaction rate with  $^1\text{O}_2$  ( $k_2$  (L-histidine,  $^1\text{O}_2$ ) =  $3.2 \times 10^7 \text{ M}^{-1} \text{ s}^{-1}$ ) [39]. Slight inhibition of the degradation of BPA was observed at a molar ratio of L-histidine to PDS of 10 (Fig. 3b). This might be due to the large consumption of PDS by L-histidine in the BC(5–1)/PDS system (Fig. S19a). Therefore, L-histidine was less suitable for the identification of  $^1\text{O}_2$  in this system. FFA is often used as a chemical probe to detect whether  $^1\text{O}_2$  exists and measure the contribution of  $^1\text{O}_2$  (Table S5). FFA was not significantly degraded in the presence of equal concentrations of FFA in the BC(5–1)/PDS system (Fig. 3d). Furthermore, the addition of FFA as a quencher to the reaction system had little effect on the degradation efficiency of BPA (Fig. 3e). It is worth mentioning that the second-order reaction rate of  $^1\text{O}_2$  with FFA is higher than that with BPA (Table S5). If  $^1\text{O}_2$  was generated, FFA would be preferentially degraded in BC(5–1)/PDS systems where FFA and BPA coexist. As exhibited in Fig. 3d, the removal efficiency of FFA was relatively low (5.8% within 30 min) and did not change with increasing concentration. In contrast, as the FFA concentration was increased from 0.1 mM to 1 mM, the degradation efficiency of BPA could still reach 94.0% within 30 min (Fig. 3e). Generally, TEMP is used as a spin trap for  $^1\text{O}_2$ . TEMPO (2,2,6,6-tetramethyl-1-piperidinyloxy) after TEMP is oxidized by  $^1\text{O}_2$  can be detected as triplet signal (1: 1: 1) by EPR [40]. Herein, a strong triplet signal also appeared in the EPR spectrum after TEMP was oxidized, and the intensity increased with time (Fig. 3f). However, based on the chemical

probe and quenching experiments of FFA, the activation process of PDS did not involve the generation of  $^1\text{O}_2$ . Therefore, the generation of the misleading triplet signal of TEMPO was not due to the oxidation of TEMP by  $^1\text{O}_2$ . Previous studies have demonstrated that TEMP loses one electron to form  $\text{TEMP}^+$ , which could also generate TEMPO after deprotonation and reaction with  $\text{O}_2$  (Fig. S19b) [41]. Moreover, solvent exchange experiments were conducted to verify the presence of  $^1\text{O}_2$  further. Generally,  $^1\text{O}_2$  has a much longer lifetime in  $\text{D}_2\text{O}$  (60  $\mu\text{s}$ ) than in  $\text{H}_2\text{O}$  (4  $\mu\text{s}$ ) [42]. Namely, the degradation rate of OMPs in  $\text{D}_2\text{O}$  will be accelerated if  $^1\text{O}_2$  is present in the system. However, the degradation rate of BPA in  $\text{D}_2\text{O}$  was not accelerated (Fig. S19c). Combined with the above experimental results, it was concluded that  $^1\text{O}_2$  was not generated during the activation of PDS in the BC(5–1)/PDS system.

Previous studies have shown that electron transfer mechanisms as another non-radical pathway might dominate the oxidation of OMPs in carbon-based PS-AOPs [20]. Therefore, the impacts of BC(5–1) and PDS premixing on the degradation performance of BPA was explored (Text S7). If free radicals and  $^1\text{O}_2$  were not generated in the system, the PDS would not be consumed by the above ROSSs during the premixing process. Conversely, premixing would result in less efficient contaminants degradation. As shown in Fig. 4a, the degradation efficiency of BPA did not decrease with the premixing of BC(5–1) and PDS but slightly increased with the premixing time. The speculation that the electron transfer regime dominated BPA oxidation was preliminarily verified [1].

In the electron transfer mechanism, surface complexes were possibly formed due to the adsorption of PDS on the catalyst surface [6]. Therefore, ATR-FTIR and Raman were performed to uncover the formation of surface complexes [43]. As exhibited in Fig. 4d, the peaks at 1273  $\text{cm}^{-1}$  and 1050  $\text{cm}^{-1}$  in FTIR spectrum of PDS were the symmetric and asymmetric vibrations of  $\text{S}=\text{O}=\text{S}$ , respectively [20]. After the addition of PDS, a new peak (1260  $\text{cm}^{-1}$ ) appeared in the FTIR spectrum of BC(5–1)/PDS, corresponding to the  $\text{S}=\text{O}=\text{S}$ , revealing the generation of PDS\* complexes on the catalyst surface. It was noteworthy that the  $\text{S}=\text{O}=\text{S}$  peak in the BC(5–1)/PDS FTIR spectra was red-shifted relative to that in pure PDS, which might be due to the lower bond energy of the  $\text{S}=\text{O}=\text{S}$  after PDS was adsorbed to BC(5–1) surface [44].

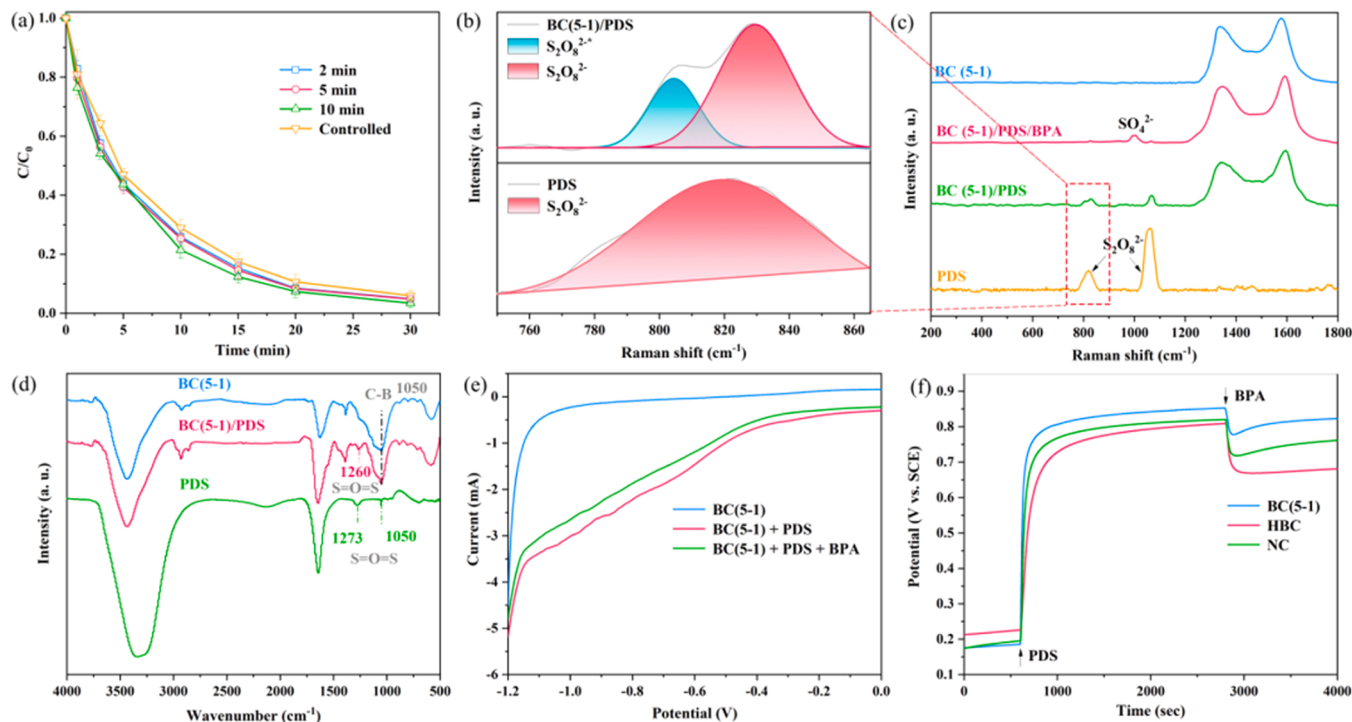


Fig. 4. (a) Premixing experiments; (b) high resolution spectroscopy of (c) Raman spectra; (d) ATR-FTIR spectra; (e) linear voltammetry curve (LSV) and (f) open circuit potential (OCP).

In Raman spectra (Fig. 4b), after dropping PDS onto the BC(5–1) surface, a new peak appeared at  $804\text{ cm}^{-1}$  ( $\text{S}_2\text{O}_8^{2-,*}$ ), which was mainly caused by the bending vibration after the peroxy bond (O–O) prolonging when PDS was adsorbed to the catalyst surface [20]. Intriguingly, when BPA was added to BC(5–1)/PDS, the peaks of  $\text{S}_2\text{O}_8^{2-}$  and  $\text{S}_2\text{O}_8^{2-,*}$  almost disappeared, while another new peak ( $\text{SO}_4^{2-}$ ) appeared around  $1002\text{ cm}^{-1}$  (Fig. 4c). The main reason for the disappearance of  $\text{S}_2\text{O}_8^{2-,*}$  might be that the metastable surface complexes ( $\text{PDS}^*$ ) formed by the adsorption of PDS on the BC(5–1) surface acted as an electron acceptor, accepted electrons from BPA as an electron donor, and then continuously consumed BPA without the generation of free radicals and  ${}^1\text{O}_2$ . Meanwhile, when PDS was adsorbed on the surface of BC(5–1), its O–O was elongated ( $\text{l}_{04-05}$  in Table S10), which was beneficial to endow PDS\* with higher activity and efficiently oxidize BPA to generate  $\text{SO}_4^{2-}$  [45].

Linear voltammetry curves (LSV) were applied to monitor the change in the current density of BC(5–1) after the addition of PDS and BPA (Text S8). As shown in Fig. 4e, the current density of BC(5–1) increased significantly after adding PDS. However, after the subsequent addition of BPA, the current density of BC(5–1) decreased slightly, suggesting that the degradation of BPA was dependent on and consumed the PDS\* formed between the PDS and the BC(5–1) surface. In addition, the equilibrium potential of BC(5–1) increased after the addition of PDS, indicating that the PDS\* possessed a higher potential (Fig. 4f, Text S8). In the open-circuit potential measurements, the potential of the glassy carbon electrode coated with catalysts increased to another potential immediately after the addition of PDS (Fig. 4f). This phenomenon further suggested that PDS adsorbed on the BC(5–1) surface and formed PDS\*. Besides, the potential difference before and after the addition of PDS was considered as the oxidation potential of PDS\* (Fig. 4f). The larger the difference, the more likely it was that BPA would be oxidized. The oxidation capacity of PDS\* formed on the surface of BC(5–1) was the highest in Fig. 4f. After adding BPA to the system, a decrease in the equilibrium potential of BC was detected, which further confirmed that the electron transfer regime dominated the PDS activation. To further illustrate the reactions occurring at a current density of LSV, chronoamperometry (CA) measurements were performed (Text S8). The CA measurement as an electrochemical analytical method can make up for the fact that LSV cannot monitor the current direction. It was worth noting that the CA voltages were set to  $0.85\text{ V}$  and  $0.18\text{ V}$ , respectively, in order to fit the OCP measurement results of BPA oxidation by PDS\* with high equilibrium potential. As shown in Fig. S20a, the reaction cell simulated the oxidation of BPA by PDS\* generated on BC(5–1) surface when the applied voltage was  $0.85\text{ V}$ . At this point, the current gradually decreased from an initial  $0.25\text{ A}$  to  $0.05\text{ A}$  over time, indicating that current flowed from the PDS\* to the BPA (Fig. S20a). When the applied voltage was below the equilibrium potential of PDS\*, the current became negative and tended to zero with time (Fig. S20a). A similar situation occurred with NC and HBC (Fig. S20b–c). The above phenomenon suggested that at a current density of LSV, PDS\* with higher potential oxidized BPA and electrons were transferred from BPA to PDS\*, thus decomposing PDS to  $\text{SO}_4^{2-}$  (Eqs. (4) and (5)).



### 3.4. Mechanistic insights into electron transfer

#### 3.4.1. Distinguish between electron shuttle and adjacent transfer

According to the conductivity of the catalyst, the electron transfer mechanism can be divided into the following two types: adjacent transfer and electron shuttle [18]. Generally, the electron transfer mechanism corresponding to conductor catalysts (carbon and precious metal, etc.) was mainly electron shuttle, while adjacent transfer may be the main electron transfer regime in semiconductor catalyst (polymeric

graphite carbon nitride and metal oxide, etc.) systems [1]. To explore whether BC(5–1) acted as an electron transfer shuttle, we constructed the electro-oxidation device presented in Fig. 5a to isolate the effect of the PDS\* on BPA degradation (Text S9). If BC(5–1) acted as an electron shuttle, electrons would be transferred from the BPA cell to the PDS cell, resulting in a significant change in the ammeter reading. As presented in Fig. 5b, except for the glassy carbon electrode without any catalyst loaded, NC, HBC, and BC(5–1) all had a significant current increase, illustrating that the catalysts acted as an electron shuttle to mediate the transfer of electrons from BPA to PDS\*. Noteworthily, after loading NC and HBC on the glassy carbon electrode, the current increased significantly at first, and then gradually decreased with time. Different from NC and HBC, the current of BC(5–1) initially increased with time and then declined gently, further suggesting that BC(5–1) exhibited the best catalytic performance, which was consistent with their respective equilibrium potentials in OCP (Fig. 4f).

#### 3.4.2. Interactions between PDS/BPA and BC

To fully get an insight into the electron transfer regime of the BC(5–1)/PDS/BPA system, the interactions between PDS/BPA and BC(5–1) were further investigated. Therefore, the effect of ionic strength (represented as  $\text{Na}_2\text{SO}_4$  concentration) on PDS adsorption on BC was carried out. The Zeta potentials of particles commonly decrease with increasing ionic strength due to its electric double layer being reduced [20]. Therefore, the ionic strength would not affect the adsorption of PDS if PDS was adsorbed on the BC(5–1) surface via inner-sphere interactions. Conversely, if PDS was adsorbed on the BC(5–1) surface through outer-sphere interactions, the quantity of PDS adsorbed decreases with increasing ionic strength. As shown in Fig. 6a–b, the ionic strength had little effect on the PDS adsorption quantity, revealing that PDS was adsorbed on the BC surface via the inner-sphere interaction. Other than that, the adsorption energies ( $E_{\text{ads}}$ ) of PDS to BC(5–1) were lower than  $-0.5\text{ eV}$ , which further confirmed that PDS was adsorbed on the surface of BC(5–1) not by physical but by chemical adsorption (Figs. S28 and S29) [46]. In addition, the new peaks of PDS\* appearing in ATR-FTIR and Raman spectra further illustrated that the adsorption of PDS on BC(5–1) was carried out through inner-sphere interactions (Fig. 4b–d) [21].

The effect of pH on the degradation performance of BPA was performed to explore the interaction between BPA and BC(5–1). This is because pH affects the Zeta potential by changing the thickness of the electric double layer on the particle surface [47,48]. The variation of the Zeta potential of BC(5–1) was not significantly influenced by PDS adsorption because PDS was adsorbed on the BC surface through the inner-sphere interaction. Therefore, the effect of pH on BPA removal efficiency might be caused by the interaction between BPA and BC(5–1). As shown in Fig. S21, the  $\text{pH}_{\text{zpc}}$  of BC(5–1) was presented as 3.1. If the interaction between BPA and BC(5–1) was electrostatic attraction, then as pH increased, BPA tended to deprotonate and increasingly repelled negatively charged BC(5–1). Intriguingly,  $k_{\text{obs}}$  showed an overall increasing trend with increasing pH (Fig. 6c–l), demonstrating that BPA was not adsorbed on BC via van der Waals interaction. Previous studies have shown that compounds containing phenolic hydroxyl groups ( $-\text{OH}$ ), such as BPA, could be adsorbed on the surface of carbonaceous materials through  $\pi$ – $\pi$  electron-donor-acceptor (EDA) interactions or hydrogen bonds [49]. Because of the resonance effect of the aromatic ring,  $\pi$  electrons could be donated by carbon atoms close to the  $-\text{OH}$  in BPA [50]. The  $-\text{COOH}$  and  $-\text{C}=\text{O}$  on the BC(5–1) surface were regarded as  $\pi$  electron acceptors due to resonance, and graphite units on BC(5–1) were considered as  $\pi$  electron donors [50]. Therefore, it was possible that EDA interactions were formed between  $-\text{OH}$  ( $\pi$  electron-donors) in BPA and  $-\text{COOH}$  and  $-\text{C}=\text{O}$  ( $\pi$  electron acceptors) on the BC(5–1) surface. The  $\text{pKa}$  of  $-\text{COOH}$  is  $\sim 3$ – $5$ . In this case, BPA was adsorbed on the BC surface by EDA interactions, and  $k_{\text{obs}}$  of BPA should be maximum at  $\text{pH}=3$ – $5$ . However, BPA had the lowest  $k_{\text{obs}}$  at  $\text{pH}=3$  (Fig. 6d and l). When pH was gradually greater than the  $\text{pKa}$  of  $-\text{COOH}$ ,

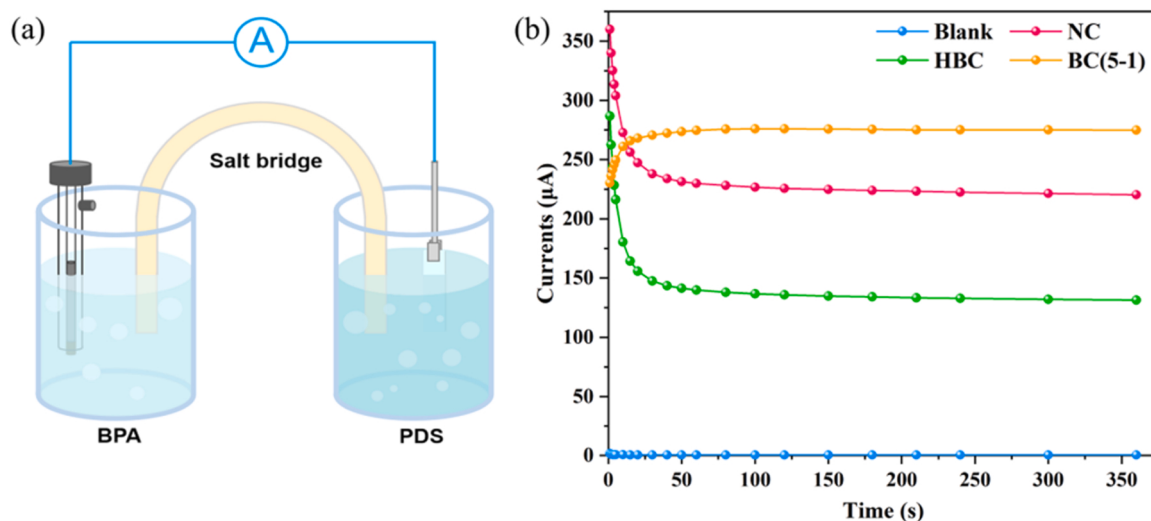


Fig. 5. (a) The electro-oxidation device and (b) current change values of the multimeter in the electro-oxidation device.

$-\text{COO}^-$  was generated on BC(5–1) surface due to deprotonation. Therefore, the charge-assisted hydrogen bonds (i. e. BC-COO $^-$ /CO $^-$ –H $^+$ –O-BPA) were produced between deprotonated  $-\text{COO}^-$ /CO $^-$  on the BC(5–1) surface and  $-\text{OH}$  of BPA. With further increase in pH,  $-\text{OH}$  on BC(5–1) surface and BPA would gradually deprotonate (pKa<sub>1</sub>, BPA = ~8, pKa<sub>2</sub>, BPA = ~9; pKa<sub>1</sub>,  $-\text{OH}$  = ~8–10 on carbonaceous materials surface) [49,50]. Meanwhile, BPA was adsorbed on the BC(5–1) surface through another charge-assisted hydrogen bond (BC-O $^-$ –H $^+$ –O-BPA). Therefore, the outer-sphere interaction existed between BPA and BC(5–1).

To further verify the adsorption of PDS and BPA on BC(5–1) surface through the inner-sphere and outer-sphere interactions, respectively, the E<sub>ads</sub> of BPA and PDS on the respective active sites of BC(5–1) surface were therefore calculated for comparison. Based on the above analysis, BPA was mainly adsorbed on  $-\text{COOH}$  and  $-\text{OH}$  to form the charge-assisted hydrogen bonds,  $-\text{COOH}$  and  $-\text{OH}$  were chosen as the active sites for the calculation. The adsorption energy of  $-0.5\text{ eV}$  is generally considered to be the critical point for both physical and chemical adsorption. The E<sub>ads</sub> of BPA on  $-\text{OH}$  and  $-\text{COOH}$  were  $-0.49$  and  $-0.45\text{ eV}$ , respectively, both higher than  $-0.5\text{ eV}$ , indicating that the physical adsorption of BPA on  $-\text{OH}$  and  $-\text{COOH}$  (Fig. S22). This calculation verified the results of the above analysis that BPA adsorbed on BC(5–1) via outer-sphere interactions. The adsorption energies of PDS on BC(5–1) were all lower than  $-0.5\text{ eV}$  compared to BPA, indicating that the catalyst surface preferentially adsorbed PDS (Fig. S28).

#### 3.4.3. Identification of the main active site

To investigate the effect of catalyst surface oxygen content on catalytic performance, HBC was thermally annealed at  $400\text{ }^\circ\text{C}$  in the air for 30, 60, 90 and 120 min. According to previous studies, the temperature interval for thermal annealing of graphite in the air was  $300$ – $500\text{ }^\circ\text{C}$ . As shown in Fig. S23, the BPA degradation efficiency decreased with increasing annealing time in air. It was noteworthy that the oxygen content on the catalyst surface increased with increasing thermal annealing time (Table S8 and Fig. S24). Moreover, as the oxygen content increased, k<sub>obs</sub> decreased (Fig. S23h).

Since NC and HBC were active for PDS, functional groups containing C and O on the catalyst surface, such as carbonyl ( $-\text{C=O}$ ), carboxyl ( $-\text{COOH}$ ) and hydroxyl ( $-\text{OH}$ ), might contribute to the activation of PDS as active sites. Before discussing the effect of functional groups, NC was verified to activate PDS through electron transfer regime (Fig. S25). To exclude the effect of the synthesis procedures on the catalytic performance, the relationship between the functional groups and k<sub>obs</sub> of a series of catalysts thermally annealed in the air were analyzed using quantitative structure-activity relationship (QSAR) (Table S8 and

Figs. S23, S24 and 26). The k<sub>obs</sub> of the catalyst decreased with increasing carboxyl and carbonyl content, indicating that the carboxyl and carbonyl hindered the BPA degradation (Fig. S26a and c). The reason for this phenomenon may be due to the fact that both carboxyl and carbonyl were strong electron-absorbing groups. Higher carboxyl and carbonyl could interfere with the  $\pi$  system and thus inhibit electron transfer. On the contrary, the apparent reaction rate increased with the increase in hydroxyl content (Fig. S26b). This may be due to the ability of the hydroxyl to increase the density of the conjugated  $\pi$  system, thus facilitating electron transfer. The correlation coefficient ( $R^2 = 0.555$ ) between C-O-C and k<sub>obs</sub> was lower, indicating that its contribution to the BPA degradation was limited (Fig. S26c).

Based on above-mentioned analysis, hydroxyl (positive correlation with oxygen content) might act as the main active site for PDS activation. However, the BPA degradation efficiency of BC(5–1), HBC and NC was negatively correlated with the oxygen content (Fig. 2a and Table S7). Therefore, the BPA and PDS adsorption experiments of BC(5–1), HBC and NC were conducted. The BPA adsorption efficiencies of NC and HBC were higher than that of BC(5–1) (Fig. S27a). However, the PDS adsorption of BC(5–1) higher than that of NC and HBC (Fig. S27b), indicating that there are other active sites besides hydroxyl that can effectively promote the adsorption and activation of PDS. The degradation performance of the carbonaceous catalysts was effectively enhanced by the incorporation of B, illustrating that B could promote the activation of PDS (Figs. 2a and S27b).

A decline in B content was observed after the reaction (Table S7). The configurations of B commonly played an important role in different boron-doped catalysts [47]. Therefore, the variations of various B species (BCO<sub>2</sub>, BC<sub>2</sub>O, and BC<sub>3</sub>) of BC(5–1) before and after the reaction were compared. The content of BC<sub>3</sub> increased, while the amount of BCO<sub>2</sub> and BC<sub>2</sub>O decreased after the reaction (Fig. 1f and Table S7). Intriguingly, BC(5–1) after the reaction was visually presented as hole-like damage (Fig. 8d–e). This may be due to the oxidative destruction of BC<sub>3</sub>, which has a graphite-like structure, leading to the generation of defective BCO<sub>2</sub> and BC<sub>2</sub>O. In addition, due to the large electronegativity difference, BCO<sub>2</sub> was more inclined to adsorb H<sub>2</sub>O. BCO<sub>2</sub> and BC<sub>2</sub>O have been shown to reduce conductivity, which was detrimental to the electron transfer process [12]. Moreover, the adsorption energies (E<sub>ads</sub>) of PDS on different configurations were calculated. Compared with other configurations, BC<sub>3</sub> exhibited the maximum E<sub>ads</sub> for PDS (Fig. S28). Hence, BC<sub>3</sub> acted as the main active site for the PDS activation, which was consistent with the study by Dou et al. [20].

The smaller value of  $\Delta E$  ( $-0.47\text{ eV}$ ) indicated that PDS was more inclined to adsorb on B-doped 2D graphitic carbon (Fig. S29).

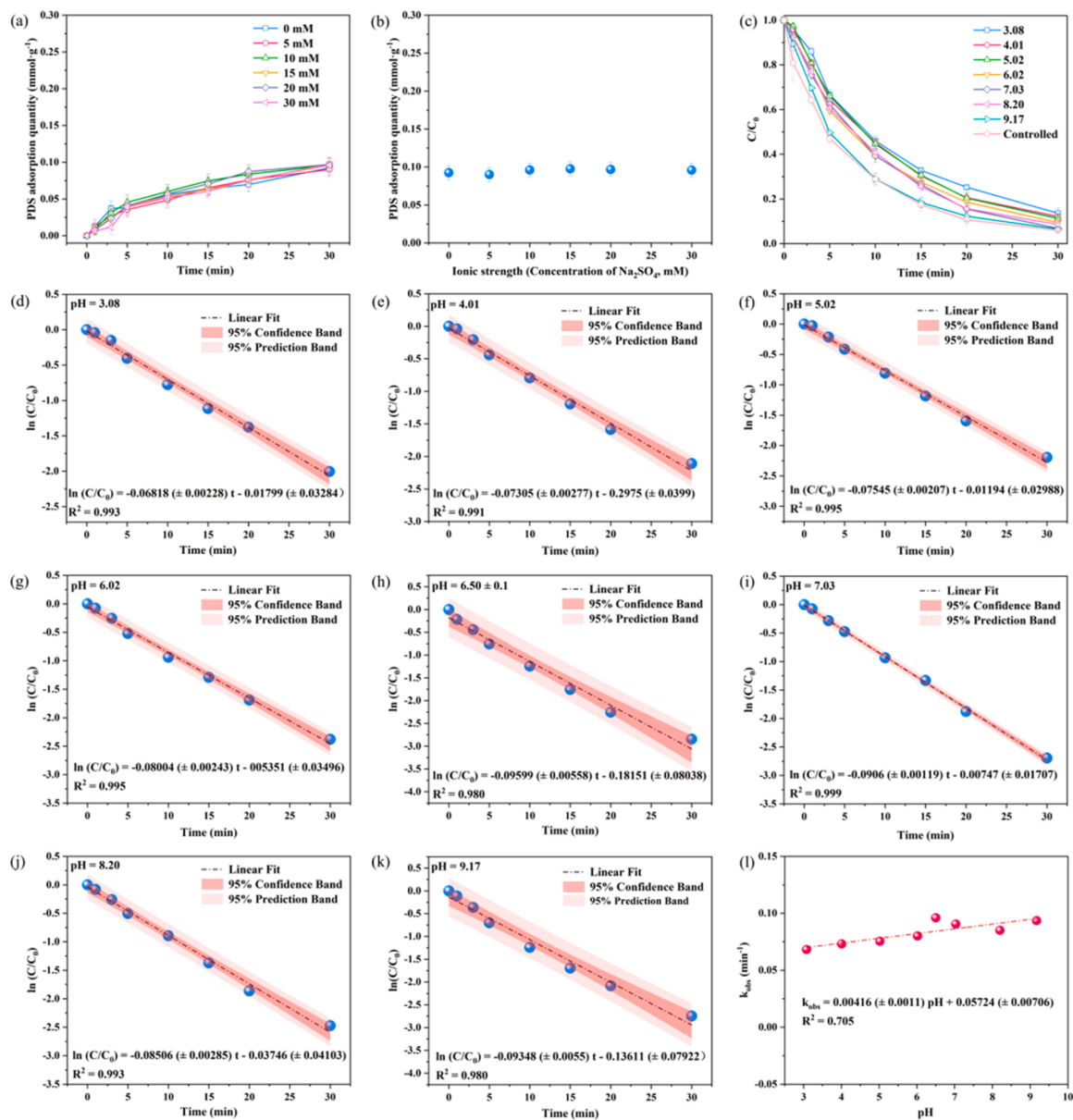


**Fig. 6.** (a-b) The effect of ionic strength on the adsorption capacity of PDS in BC(5–1)/PDS system; (c) Effect of pH on BPA degradation; (d-k) Plots of  $\ln(C/C_0)$  versus time for the degradation of BPA under different pH conditions; (l) Correlation of  $k_{\text{obs}}$  to pH. Reaction conditions: [BPA] = 0.1 mM, [PDS] = 3 mM, [catalyst] = 0.1 g/L, [temp] =  $23 \pm 2$  °C, initial pH =  $6.5 \pm 0.1$ .

Furthermore, the adsorption energy of PDS\* on B-doped 2D graphitic carbon was more negative than that on 2D graphitic carbon, which demonstrated that electrons preferred to transfer from BPA to PDS\* on B-doped 2D graphitic carbon (Fig. S29). Therefore, the doping of B could effectively improve the electron transfer properties, especially BC<sub>3</sub>, and thus elevated the BPA degradation performance. Bard charge analysis was performed to calculate the effective charge of 2D graphitic carbon with/without B doping to reveal the charge transfer process. Since the electronegativity of C was greater than that of B, the electrons around B transferred to the surrounding C atoms when B was doped in the 2D graphitic carbon network (Fig. 7 and Tables S9–S11). After adsorption of PDS molecules, the Bader charge of active sites B<sub>1</sub>, C<sub>27</sub>, C<sub>28</sub>, and C<sub>39</sub> decreased 0.04, 0.046, 0.067, and 0.064 eV, respectively, indicating that electrons were transferred from the BC<sub>3</sub> site to PDS (Fig. 7b, d, and Tables S9 and S10). Moreover, the O–O bond was elongated ( $\text{I}_{\text{O4–O5}} = 1.503 \text{ \AA}$  vs.  $1.485 \text{ \AA}$ ) after the PDS accepted electrons from the BC<sub>3</sub> site, making the metastable surface complex more active, which was consistent with the Raman spectra analyses (Table S10, Fig. 4b–c).

### 3.5. Evaluation of catalytic performance and stability

Removal experiments of different phenolic OMPs were conducted to evaluate the selective removal performance of the BC(5–1)/PDS system. As shown in Figs. S30 and 8b, phenolic pollutants presented higher pseudo-first-order reaction rates in BC(5–1)/PDS system. Since ionization potential is commonly used to measure the redox ability of organic compounds, the relationship between the above OMPs and ionization energy (IE) was further investigated [36]. Consistent with previous studies, there was a threshold for the removal ability of OMPs with different IE in PS-AOPs dominated by the electron transfer regime [51]. In BC(5–1)/PDS system, the OMPs had an IE threshold of approximately 9.38 (Fig. 8b).

Furthermore, we investigated mineralization efficiency by measuring total organic carbon (TOC) in samples at certain time intervals, which was also used as an indicator of OMPs removal performance. Unexpectedly, the TOC removal efficiency reached 76.0% within 30 min, illustrating that the BC(5–1)/PDS system exhibited excellent

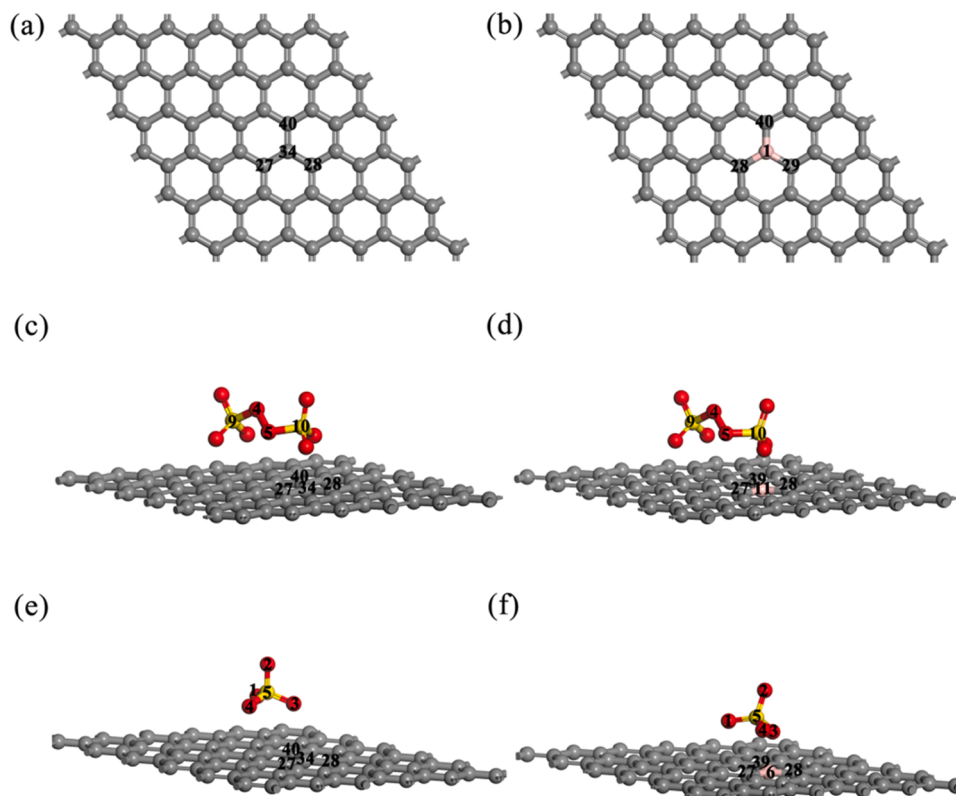


**Fig. 7.** Bader charge of (a) 2D graphitic carbon, (b) B-doped 2D graphitic carbon, (c) 2D graphitic carbon adsorbed by PDS, (d) B-doped 2D graphitic carbon adsorbed by PDS, (e) 2D graphitic carbon adsorbed by  $\text{SO}_4^*$  and (d) B-doped 2D graphitic carbon adsorbed by  $\text{SO}_4^*$ .

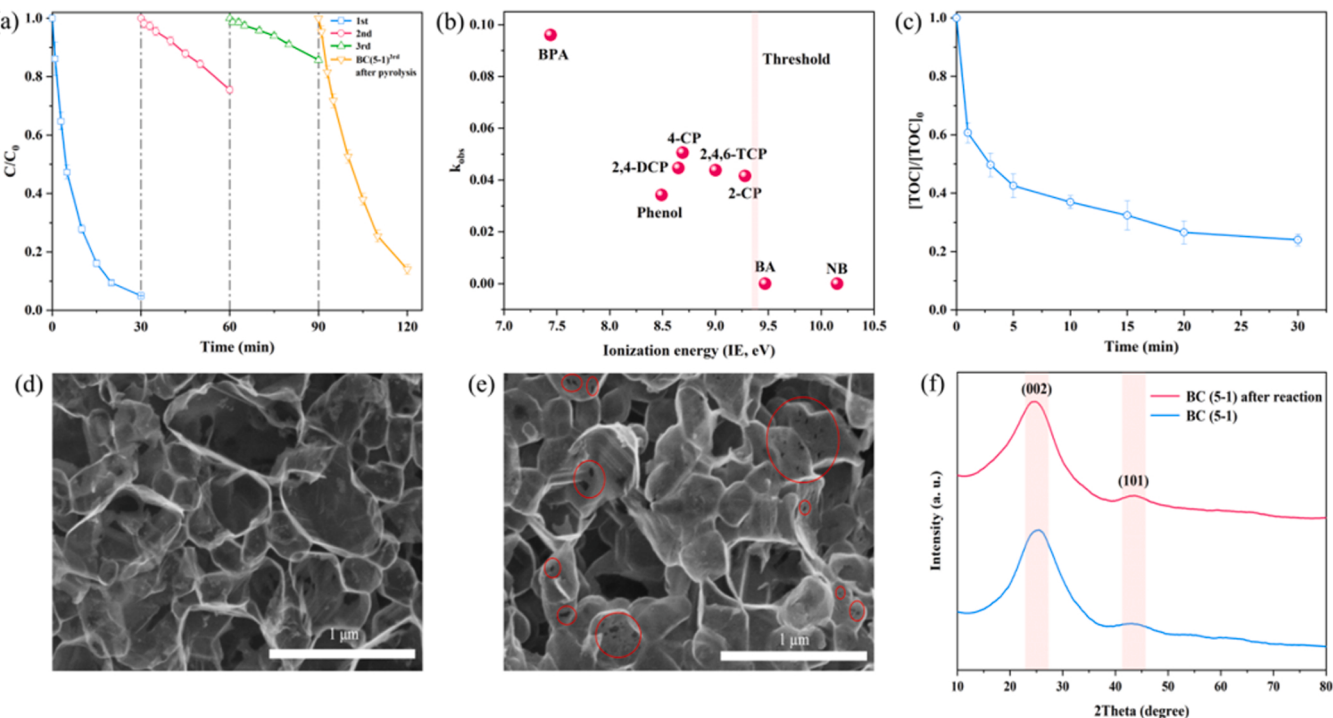


**Fig. 8.** (a) Reusability experiments; (b) Selective degradation in BC(5–1)/PDS system; (c) The mineralization performance of BC(5–1)/PDS system; Comparison of SEM images of BC(5–1) (d) before and (e) after the reaction; Comparison of (f) XRD pattern of BC(5–1) before and after reaction. Reaction conditions: [BPA] = [Phenol] = [2,4-DCP] = [2,4,6-TCP] = [2-CP] = [BA] = [NB] = [0.1 mM], [PDS] = 3 mM, [catalyst] = 0.1 g/L, [temp] =  $23 \pm 2^\circ\text{C}$ .

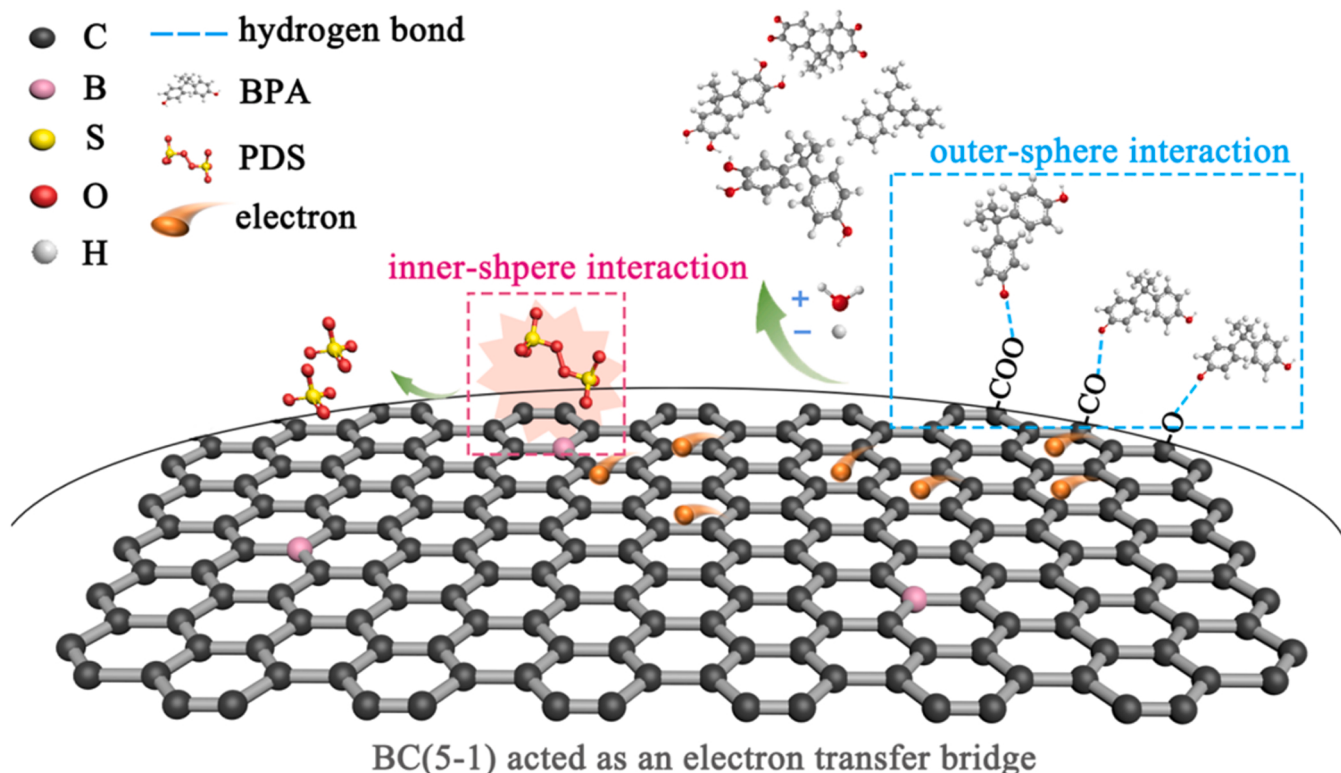
mineralization performance to OMPs (Fig. 8c). However, the BC(5–1) used in the second (24.5% in 30 min) and third (14.3% in 30 min) cycles have poor performance in degrading BPA under the same conditions (Fig. 8a). It was possible that the main active site for adsorbing PDS, BC<sub>3</sub>, was irreversibly inactivated by oxidation (Figs. 1f and S28). As shown in Table S7 and Fig. S6c, the oxygen content on the surface of BC(5–1) increased after the first reaction. Although the BC(5–1) still maintained the graphite phase structure after the reaction, the 2D graphitic carbon sheet visually presented as hole-like damage after the main active sites on the catalyst surface were oxidized (Fig. 8d-f). In addition, the BC(5–1) after the 3rd cycle was pyrolyzed at 800 °C for 2 h in Ar, and then reused to activate PDS to remove BPA. As exhibited in Fig. 8a, the pyrolyzed catalyst significantly improved the BPA degradation efficiency (86% in 30 min) compared with the 2nd and 3rd reusability experiments, further illustrating that the oxidation of the main active site led to irreversible deactivation. The intensity ratio of the two characteristic peaks of D-band and G-band in Raman spectra, namely  $I_D/I_G$ , is commonly employed to describe the disorder and defect degree of carbonaceous materials [25]. The  $\pi$  electrons in the localized region defects could be liberated from the conjugated network and become charge transfer sites, which was beneficial to improving the conductivity of carbonaceous materials [52]. However, excess defects can destroy the conjugated  $\pi$  structure of the carbon network, resulting in a slow charge transfer rate [53]. The ratio of  $I_D/I_G$  rose from 0.87 to 1.09, manifested the increase in defect content after the reaction led to poor conductivity, which reduced the BPA degradation performance dominated by the electron transfer regime (Fig. S31).

Based on the above analysis, a possible mechanism was proposed in the BC(5–1)/PDS/BPA system (Scheme 1). First, PDS adsorbed on BC(5–1) via inner-sphere interactions to form metastable surface complexes (PDS\*), which could extract electrons from the active sites on BC(5–1). Simultaneously, BPA and BC(5–1) were also connected by outer-sphere interactions. Next, electrons would be transferred from BPA acted as the electron donor to the PDS\* through BC(5–1) as an electron shuttle, resulting in the degradation of BPA without generating free

radicals and  $^1\text{O}_2$ .

### 3.6. Degradation pathways

The intermediates during the degradation of BPA were analyzed by LC-MS. Details of the intermediates were shown in Table S12. On the foundation of mass spectra analysis, three possible BPA degradation pathways were proposed (Figs. 9 and S31) [54,55]. In the electron transfer pathway, electrons were transferred from electron-rich BPA to PDS\* via BC(5–1) as an electron transfer bridge. After the addition of BPA reduced the equilibrium potential of the PDS\*, BPA exhibited an electron-deficient state. BPA first interacted with water molecules to form hydroxylation products (dihydroxylated BPA, P1,  $m/z$  = 260 and monohydroxylated BPA, P2,  $m/z$  = 243) and P3 in the presence of PDS\* (pathway 1–3). The hydroxyl groups on P1 were further oxidized to carbonyl to generate P4,  $m/z$  = 255. P7 ( $m/z$  = 246) was possibly produced by the sequential electron transfer reactions of P1 and P4 with the PDS\*. In another hydroxylation pathway (Pathway 2), 2-(4-hydroxyphenyl)-propanol-2-ol (P5,  $m/z$  = 151) and (1-trimethylmethane-3-hydroxyl-5-carbonyl)-1,5-cyclohexadiene (P6,  $m/z$  = 165) were generated after  $\beta$ -rupture between two benzene rings in P2, which were transferred into p-isopropenyl phenol (P8,  $m/z$  = 135) and (1-isopropenyl-3-hydroxyl-5-carbonyl)-1,5-cyclohexadiene (P9,  $m/z$  = 149), respectively. P8 was further oxidized to p-hydroxybenzaldehyde (P11,  $m/z$  = 121) and p-hydroxybenzoic acid (P12,  $m/z$  = 137) due to the loss of electrons. Besides, (1-phenyl-1-butene) benzene (P3,  $m/z$  = 208) was also detected as one of the intermediate products of BPA degradation. Subsequently, the above intermediate underwent ring-opening cleavage to produce succinic acid (P13,  $m/z$  = 117), 1-propene-8-hydroxyl-allyl oxalate (P14,  $m/z$  = 187), 1-hexene-3,4-dione-6-hydroxyl (P15,  $m/z$  = 128), divinyloxyethane (P16,  $m/z$  = 113), 1-butyl propene oxalate (P17,  $m/z$  = 171) and maleic acid (P18,  $m/z$  = 116). The ring-opened small molecules were eventually converted into  $\text{CO}_2$  and  $\text{H}_2\text{O}$ .



Scheme 1. Proposed mechanistic insights in BC(5–1)/PDS/BPA system.

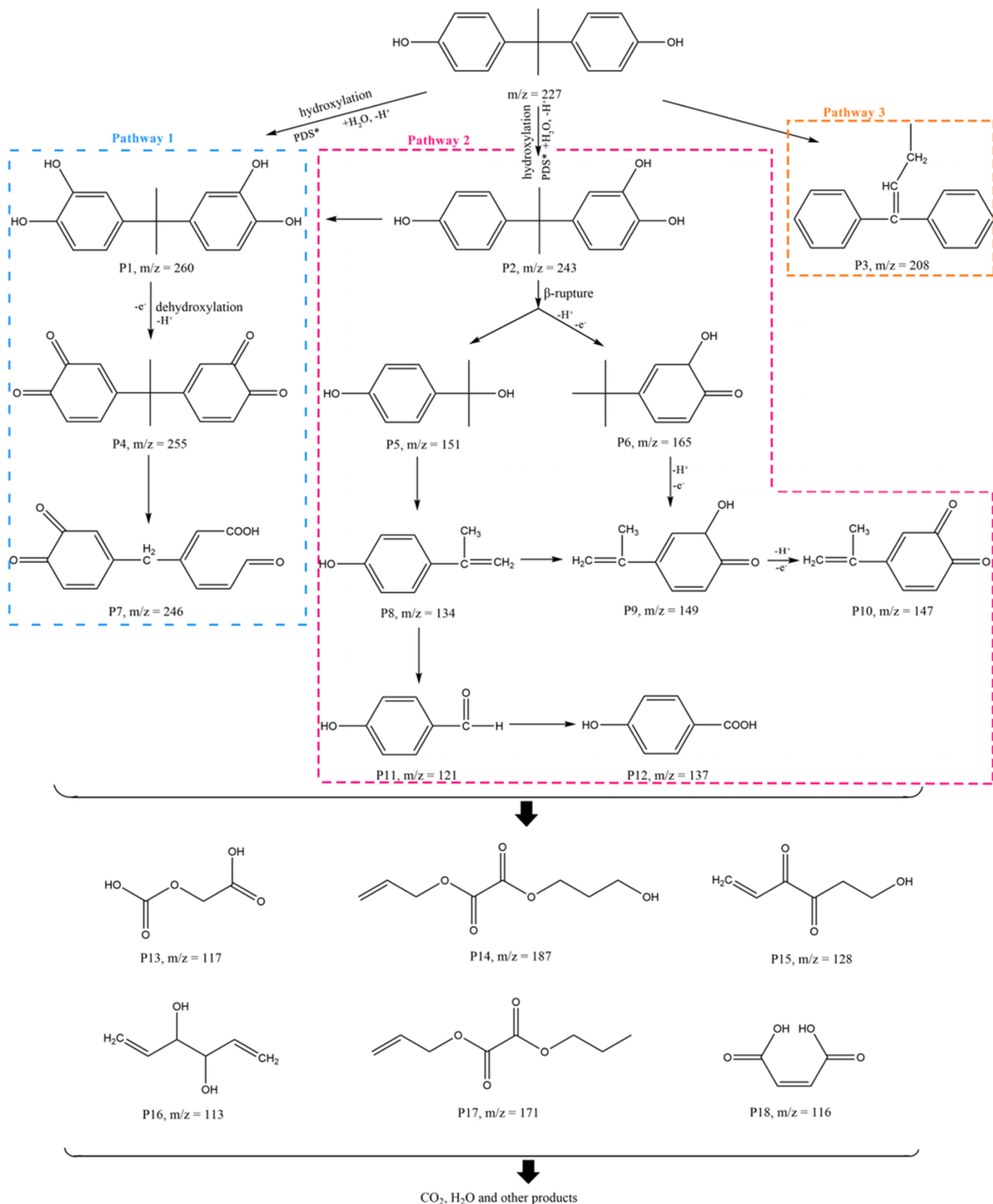


Fig. 9. The possible pathways during BPA degradation in BC(5-1)/PDS system.

#### 4. Conclusion

Overall, we have conducted an in-depth exploration of the mechanism of PDS activation by B-doped metal-free carbonaceous materials.

Multiple experimental results demonstrate that BC(5-1) activate PDS through electron transfer mediated by the catalyst itself as an electron transfer shuttle without involving any radical ROSs. Furthermore, we further investigated the interactions between PDS/BPA and BC(5-1).

On the one hand, it was found that PDS adsorbed on BC(5–1) through inner-sphere interaction, resulting in the generation of metastable surface complexes, which improved the equilibrium potential of the catalyst surface and was more conducive to the removal of BPA. On the other hand, the interaction between BPA and BC(5–1) was shown to be outer-sphere interactions dominated by charge-assisted hydrogen bonding at different pH conditions. Other than that, the doping of B could effectively elevate the PDS activation performance and BC<sub>3</sub> was validated as the main active site. This work is devoted to an in-depth study of the electron transfer regime, interactions present in the reaction system, and the main active site during the activation of PDS by B-doped metal-free carbonaceous materials, which can provide another novel perspective on the PS-AOPs dominated by non-radical pathways. Compared with previous work on the persulfate activation by B-doped carbonaceous materials, the relatively high B-doping and relatively low O-doping resulted in better conductivity of the catalyst, which effectively improved the removal and mineralization efficiency of OMPs. However, it was precisely because BC<sub>3</sub> was the main active site and was continuously oxidized during the activation process, resulting in poor reusability. Therefore, it will be another breakthrough if the oxidation of the catalyst can be retarded to elevate the reusability efficiency in the future.

#### CRediT authorship contribution statement

**Meng-Zhu Qin:** Conceptualization, Methodology, Validation, Formal analysis, Investigation, Data curation, Writing – original draft, Writing – review & editing, Visualization. **Yanyan Bian:** Visualization, Supervision, Writing – review & editing. **Huai-Yuan Niu:** Supervision. **Wen-Xin Fu:** Supervision. **Xue-Gang Zhang:** Supervision. **Qi-Yao Hu:** Supervision. **Duan Guo:** Supervision. **Cheng-Gang Niu:** Supervision, Writing – review & editing. **Lei Zhang:** Supervision.

#### Declaration of Competing Interest

The authors declare that they have no known competing financial interests or personal relationships that could have appeared to influence the work reported in this work.

#### Data availability

Data will be made available on request.

#### Acknowledgments

This work was financially supported by the National Natural Science Foundation of China (U22A20606), the Scientific research projects of Department of the Ecology and Environment of Hunan Province (HBKT-2021030), the Key Scientific Research Project of the Department of Education of Hunan Province (21A0015).

#### Appendix A. Supplementary material

Supplementary data associated with this article can be found in the online version at [doi:10.1016/j.apcatb.2022.122285](https://doi.org/10.1016/j.apcatb.2022.122285).

#### References

- [1] W. Ren, C. Cheng, P. Shao, X. Luo, H. Zhang, S. Wang, X. Duan, Origins of electron-transfer regime in persulfate-based nonradical oxidation processes, *Environ. Sci. Technol.* 56 (2022) 78–97.
- [2] X. Xiong, Z. Wang, Y. Zhang, Z. Li, R. Shi, T. Zhang, Wettability controlled photocatalytic reactive oxygen generation and *Klebsiella pneumoniae* inactivation over triphase systems, *Appl. Catal. B* 264 (2020), 118518.
- [3] X.Q. Jia, X.Y. Bai, Z.Z. Ji, Y. Li, Y. Sun, X.Y. Mi, S.H. Zhan, Insight into the effective removal of ciprofloxacin using a two-dimensional layered NiO/g-C<sub>3</sub>N<sub>4</sub> composite in Fe-free photo-electro-Fenton system, *Acta Phys. Chim. Sin.* 37 (2021), 2010042-0.
- [4] W.Y. Peng, Y.X. Dong, Y. Fu, L.L. Wang, Q.C. Li, Y.J. Liu, Q.Y. Fan, Z.H. Wang, Non-radical reactions in persulfate-based homogeneous degradation processes: a review, *Chem. Eng. J.* 421 (2021), 127818.
- [5] Y. Zhao, L. Yu, C. Song, Z. Chen, F. Meng, M. Song, Selective Degradation of electron-rich organic pollutants induced by CuO@Biochar: the key role of outer-sphere interaction and singlet oxygen, *Environ. Sci. Technol.* 56 (2022) 10710–10720.
- [6] W. Ren, L. Xiong, G. Nie, H. Zhang, X. Duan, S. Wang, Insights into the electron-transfer regime of peroxydisulfate activation on carbon nanotubes: the role of oxygen functional groups, *Environ. Sci. Technol.* 54 (2020) 1267–1275.
- [7] S. Cai, Q. Zhang, Z.Q. Wang, S. Hua, D.H. Ding, T.M. Cai, R.H. Zhang, Pyrrolic N-rich biochar without exogenous nitrogen doping as a functional material for bisphenol A removal: performance and mechanism, *Appl. Catal. B* 291 (2021), 120093.
- [8] H.Y. Luo, H.Y. Fu, H. Yin, Q.T. Lin, Carbon materials in persulfate-based advanced oxidation processes: the roles and construction of active sites, *J. Hazard. Mater.* 426 (2022), 128044.
- [9] J. Ortiz-Medina, Z.P. Wang, R. Cruz-Silva, A. Morelos-Gomez, F. Wang, X.D. Yao, M. Terrones, M. Endo, Defect engineering and surface functionalization of nanocarbons for metal-free catalysis, *Adv. Mater.* 31 (2019), 1805717.
- [10] Y. Gao, Z. Chen, Y. Zhu, T. Li, C. Hu, New insights into the generation of singlet oxygen in the metal-free peroxyomonosulfate activation process: important role of electron-deficient carbon atoms, *Environ. Sci. Technol.* 54 (2020) 1232–1241.
- [11] C. Wang, Z.Y. Guo, W. Shen, Q.J. Xu, H.M. Liu, Y.G. Wang, B-doped carbon coating improves the electrochemical performance of electrode materials for Li-ion batteries, *Adv. Funct. Mater.* 24 (2014) 5511–5521.
- [12] T.V. Tam, S.G. Kang, M.H. Kim, S.G. Lee, S.H. Hur, J.S. Chung, W.M. Choi, Novel graphene hydrogel/B-doped graphene quantum dots composites as trifunctional electrocatalysts for Zn-air batteries and overall water splitting, *Adv. Energy Mater.* 9 (2019), 1900945.
- [13] J. Han, L.L. Zhang, S. Lee, J. Oh, K.S. Lee, J.R. Potts, J. Ji, X. Zhao, R.S. Ruoff, S. Park, Generation of B-doped graphene nanoplatelets using a solution process and their supercapacitor applications, *ACS Nano* 7 (2013) 19–26.
- [14] B.H. Liu, W.Q. Guo, H.Z. Wang, Q.S. Si, Q. Zhao, H.C. Luo, N.Q. Ren, B-doped graphitic porous biochar with enhanced surface affinity and electron transfer for efficient peroxydisulfate activation, *Chem. Eng. J.* 390 (2020).
- [15] S. Gao, Z. Wang, H. Wang, Y. Jia, N. Xu, X. Wang, J. Wang, C. Zhang, T. Tian, W. Shen, Peroxydisulfate activation using B-doped biochar for the degradation of oxytetracycline in water, *Appl. Surf. Sci.* 599 (2022), 153917.
- [16] Y.B. Wang, M. Liu, X. Zhao, D. Cao, T. Guo, B. Yang, Insights into heterogeneous catalysis of peroxyomonosulfate activation by boron-doped ordered mesoporous carbon, *Carbon* 135 (2018) 238–247.
- [17] X. Li, D. Liang, C. Wang, Y. Li, Insights into the peroxyomonosulfate activation on boron-doped carbon nanotubes: performance and mechanisms, *Chemosphere* 275 (2021), 130058.
- [18] P.J. Duan, X. Xu, K.Y. Guo, Q.Y. Yue, B.Y. Gao, Peroxyomonosulfate activation on a chainmail catalyst via an electron shuttle mechanism for efficient organic pollutant removal, *Appl. Catal. B* 316 (2022), 121695.
- [19] Q. Yang, Y. Chen, X. Duan, S. Zhou, Y. Niu, H. Sun, L. Zhi, S. Wang, Unzipping carbon nanotubes to nanoribbons for revealing the mechanism of nonradical oxidation by carbocatalysis, *Appl. Catal. B* 276 (2020), 119146.
- [20] J. Dou, J. Cheng, Z. Lu, Z. Tian, J. Xu, Y. He, Biochar co-doped with nitrogen and boron switching the free radical based peroxydisulfate activation into the electron-transfer dominated nonradical process, *Appl. Catal. B* 301 (2022), 120832.
- [21] T. Zhang, Y. Chen, Y. Wang, J. Le Roux, Y. Yang, J.P. Croué, Efficient peroxydisulfate activation process not relying on sulfate radical generation for water pollutant degradation, *Environ. Sci. Technol.* 48 (2014) 5868–5875.
- [22] S. Goldberg, Chemistry of the solid-water interface processes at the mineral-water and particle-water interface in natural systems, *Soil Sci.* 156 (1993).
- [23] E.L. Christian, V.E. Anderson, M.E. Harris, Deconvolution of Raman spectroscopic signals for electrostatic, H-bonding, and inner-sphere interactions between ions and dimethyl phosphate in solution, *J. Inorg. Biochem.* 105 (2011) 538–547.
- [24] M. Huang, Y. Han, W. Xiang, D. Zhong, C. Wang, T. Zhou, X. Wu, J. Mao, In situ-formed phenoxyl radical on the CuO surface triggers efficient persulfate activation for phenol degradation, *Environ. Sci. Technol.* 55 (2021) 15361–15370.
- [25] Y. Liu, J. Luo, L. Tang, C. Feng, J. Wang, Y. Deng, H. Liu, J. Yu, H. Feng, J. Wang, Origin of the enhanced reusability and electron transfer of the carbon-coated Mn<sub>2</sub>O<sub>4</sub> nanocube for persulfate activation, *ACS Catal.* 10 (2020) 14857–14870.
- [26] H. Lee, H.J. Lee, J. Jeong, J. Lee, N.B. Park, C. Lee, Activation of persulfates by carbon nanotubes: oxidation of organic compounds by nonradical mechanism, *Chem. Eng. J.* 266 (2015) 28–33.
- [27] C.J. Liang, C.F. Huang, N. Mohanty, R.M. Kurakalva, A rapid spectrophotometric determination of persulfate anion in ISCO, *Chemosphere* 73 (2008) 1540–1543.
- [28] W. Wang, L. Shang, G.J. Chang, C.Y. Yan, R. Shi, Y.X. Zhao, G.I.N. Waterhouse, D. J. Yang, T.R. Zhang, Intrinsic carbon-defect-driven electrocatalytic reduction of carbon dioxide, *Adv. Mater.* 31 (2019), 1808276.
- [29] J.L. Yang, Z.C. Ju, Y. Jiang, Z. Xing, B.J. Xi, J.K. Feng, S.L. Xiong, Enhanced capacity and rate capability of nitrogen/oxygen dual-doped hard carbon in capacitive potassium-ion storage, *Adv. Mater.* 30 (2018), 1700104.
- [30] X.G. Duan, C. Su, J. Miao, Y.J. Zhong, Z.P. Shao, S.B. Wang, H.Q. Sun, Insights into perovskite-catalyzed peroxyomonosulfate activation: maneuverable cobalt sites for promoted evolution of sulfate radicals, *Appl. Catal. B* 220 (2018) 626–634.
- [31] M.D. Donohue, G.L. Aranovich, Classification of Gibbs adsorption isotherms, *Adv. Colloid Interface Sci.* 76–77 (1998) 137–152.

[32] W. Ren, P. Zhou, G. Nie, C. Cheng, X. Duan, H. Zhang, S. Wang, Hydroxyl radical dominated elimination of plasticizers by peroxymonosulfate on metal-free boron: kinetics and mechanisms, *Water Res.* 186 (2020), 116361.

[33] X.G. Duan, W.L. Li, Z.M. Ao, J. Kang, W.J. Tian, H.Y. Zhang, S.H. Ho, H.Q. Sun, S. B. Wang, Origins of boron catalysis in peroxymonosulfate activation and advanced oxidation, *J. Mater. Chem. A* 7 (2019) 23904–23913.

[34] C.Y. Nie, Z.H. Dai, W.J. Liu, X.G. Duan, C.Y. Wang, B. Lai, Z.M. Ao, S.B. Wang, T. C. An, Criteria of active sites in nonradical persulfate activation process from integrated experimental and theoretical investigations: boron-nitrogen-co-doped nanocarbon-mediated peroxydisulfate activation as an example, *Environ. Sci. Nano* 7 (2020) 1899–1911.

[35] F. Li, Z. Lu, T. Li, P. Zhang, C. Hu, Origin of the excellent activity and selectivity of a single-atom copper catalyst with unsaturated Cu-N<sub>2</sub> sites via peroxydisulfate activation: Cu(III) as a dominant oxidizing species, *Environ. Sci. Technol.* 56 (2022) 8765–8775.

[36] S. Zhu, X. Li, J. Kang, X. Duan, S. Wang, Persulfate activation on crystallographic manganese oxides: mechanism of singlet oxygen evolution for nonradical selective degradation of aqueous contaminants, *Environ. Sci. Technol.* 53 (2019) 307–315.

[37] Y. Bu, H. Li, W. Yu, Y. Pan, L. Li, Y. Wang, L. Pu, J. Ding, G. Gao, B. Pan, Peroxydisulfate activation and singlet oxygen generation by oxygen vacancy for degradation of contaminants, *Environ. Sci. Technol.* 55 (2021) 2110–2120.

[38] J. Yu, L. Tang, Y. Pang, G. Zeng, H. Feng, J. Zou, J. Wang, C. Feng, X. Zhu, X. Ouyang, J. Tan, Hierarchical porous biochar from shrimp shell for persulfate activation: a two-electron transfer path and key impact factors, *Appl. Catal. B* 260 (2020), 118160.

[39] Z. Yang, Z. Wang, G. Liang, X. Zhang, X. Xie, Catalyst bridging-mediated electron transfer for nonradical degradation of bisphenol A via natural manganese ore-cornstalk biochar composite activated peroxymonosulfate, *Chem. Eng. J.* 426 (2021), 131777.

[40] K.C. Das, C.K. Das, Curcumin (diferuloylmethane), a singlet oxygen (<sup>1</sup>O<sub>2</sub>) quencher, *Biochem. Biophys. Res. Commun.* 295 (2002) 62–66.

[41] G. Nardi, I. Manet, S. Monti, M.A. Miranda, V. Lhiaubet-Vallet, Scope and limitations of the TEMPO/EPR method for singlet oxygen detection: the misleading role of electron transfer, *Free Radic. Biol. Med.* 77 (2014) 64–70.

[42] M. Scholz, R. Dedic, T. Breitenbach, J. Hala, Singlet oxygen-sensitized delayed fluorescence of common water-soluble photosensitzers, *Photochem. Photobiol. Sci.* 12 (2013) 1873–1884.

[43] X. Miao, X. Chen, W. Wu, D. Lin, K. Yang, Intrinsic defects enhanced biochar/peroxydisulfate oxidation capacity through electron-transfer regime, *Chem. Eng. J.* 438 (2022), 135606.

[44] J. Liu, Z. Zhao, P. Shao, F. Cui, Activation of peroxymonosulfate with magnetic Fe<sub>3</sub>O<sub>4</sub>–MnO<sub>2</sub> core–shell nanocomposites for 4-chlorophenol degradation, *Chem. Eng. J.* 262 (2015) 854–861.

[45] W. Ren, L. Xiong, X. Yuan, Z. Yu, H. Zhang, X. Duan, S. Wang, Activation of peroxydisulfate on carbon nanotubes: electron-transfer mechanism, *Environ. Sci. Technol.* 53 (2019) 14595–14603.

[46] P. Zhang, Y. Yang, X. Duan, Y. Liu, S. Wang, Density functional theory calculations for insight into the heterocatalyst reactivity and mechanism in persulfate-based advanced oxidation reactions, *ACS Catal.* 11 (2021) 11129–11159.

[47] Y.D. Chen, X.G. Duan, C.F. Zhang, S.B. Wang, N.Q. Ren, S.H. Ho, Graphitic biochar catalysts from anaerobic digestion sludge for nonradical degradation of micropollutants and disinfection, *Chem. Eng. J.* 384 (2020), 123244.

[48] L. Zhang, P. Fang, L. Yang, J. Zhang, X. Wang, Rapid method for the separation and recovery of endocrine-disrupting compound bisphenol AP from wastewater, *Langmuir* 29 (2013) 3968–3975.

[49] M.B. Ahmed, J.L. Zhou, H.H. Ngo, M.A.H. Johir, K. Sornalingam, Sorptive removal of phenolic endocrine disruptors by functionalized biochar: competitive interaction mechanism, removal efficacy and application in wastewater, *Chem. Eng. J.* 335 (2018) 801–811.

[50] F.F. Liu, J. Zhao, S. Wang, P. Du, B. Xing, Effects of solution chemistry on adsorption of selected pharmaceuticals and personal care products (PPCPs) by graphenes and carbon nanotubes, *Environ. Sci. Technol.* 48 (2014) 13197–13206.

[51] G. Liu, H. Yu, T. Zhou, R. Jin, J. Zhou, Activation of peroxydisulfate by biogenic nanocomposites of reduced graphene oxide and goethite for non-radical selective oxidation of organic contaminants: Production of singlet oxygen and direct electron transfer, *Chem. Eng. J.* 430 (2022), 133177.

[52] M. Yang, Z. Zhou, Recent breakthroughs in supercapacitors boosted by nitrogen-rich porous carbon materials, *Adv. Sci.* 4 (2017), 1600408.

[53] W.Y. Zhang, J.X. Zhu, H.X. Ang, Y. Zeng, N. Xiao, Y.B. Gao, W.L. Liu, H.H. Hng, Q. Y. Yan, Binder-free graphene foams for O<sub>2</sub> electrodes of Li–O<sub>2</sub> batteries, *Nanoscale* 5 (2013) 9651–9658.

[54] W.D. Oh, Z. Wong, X. Chen, K.Y.A. Lin, A. Veksha, G. Lisak, C. He, T.T. Lim, Enhanced activation of peroxydisulfate by CuO decorated on hexagonal boron nitride for bisphenol A removal, *Chem. Eng. J.* 393 (2020), 124714.

[55] C. Li, X.Z. Li, N. Graham, N.Y. Gao, The aqueous degradation of bisphenol A and steroid estrogens by ferrate, *Water Res.* 42 (2008) 109–120.